

Chapter 3

Power Spectrum and its Applications

3.1. Introduction

The spectrum of a homogeneous random field is a most useful property; indeed if the random field is Gaussian, it completely characterises the random field. This chapter is devoted to the study of the spectrum of potential fields. Sections 3.2 and 3.3 introduce spectrum and other functions such as radial spectrum, angular spectrum, cross-spectrum, coherence, transfer function, etc. and the role of sampling and quantization on the spectrum. In Section 3.3 computational aspects are covered. The basic tool for the spectrum estimation is 2D discrete Fourier transform. A brief discussion on bias and variance is included. The applications of spectrum are covered in the next three sections. The most interesting application of the spectrum is in the estimation of depth variation of magnetization, in particular, ‘spectral depths’ from the radial spectrum. The angular spectrum is useful for obtaining directional information such as on polarization, faults and other structural features. Finally, the last section is devoted to the study of coherence between gravity and magnetic fields and between gravity and topography for isostatic compensation.

3.2. Spectrum of random fields

Most geophysical fields, in particular gravity and magnetic fields, are caused by an ensemble of sources distributed in some complex manner, which may best be described in a stochastic framework. Then, the resulting potential field measured on the surface is characterized by a random function of two spatial coordinates. The stochastic model is particularly useful in the study of a large map as a whole, but not in bits and pieces. The statistical approach was first advocated by Horton et al. [1] in 1964 and later by Mundt [2] in 1968. The theory of random fields may be found in many books on stochastic processes, for example, the book by Yaglom is strongly recommended [3]. The spectral theory of stochastic processes is well documented (see, for example, a recent text [4]). However, the spectral theory of two-dimensional random fields is not dealt with in most books.

For this reason we briefly review the spectral theory of 2D random fields emphasizing those points where the spectral theory of 2D fields differs from that of time series [4].

3.2.1. Random functions (2D)

When a continuous random variable becomes a function of two spatial coordinates a random function in two dimensions is realized. Conversely, a random function observed at a fixed point in a plane is a random variable. The more familiar stochastic process is a random function where the independent variable is time. In potential field characterization we take the view point that the potential field, being the result of randomly distributed large number of sources, is best modeled as a random function. In this process we do not look at the microscopic variations but rather at the macroscopic or broad picture of the source distribution. A random function may be characterized by means of a few quantities particularly when it is a homogeneous function which is also known as the stationary function for a stochastic process.

3.2.2. Autocorrelation and cross-correlation

A homogeneous random field measured at two points, namely, at (x_1, y_1) and (x_2, y_2) may be related to each other through a covariance function, defined as follows:

$$C_f(\Delta x, \Delta y) = E\{(f(x_1, y_1) - m_f)(f(x_2, y_2) - m_f)\} \quad (3.1)$$

where $\Delta x = x_2 - x_1$ and $\Delta y = y_2 - y_1$. Here we have shown that the covariance function is a function of the difference in the spatial coordinates. This, indeed, is a special case of great importance. Such a random field is known as a homogeneous (also called stationary) random field. The mean and variance of a homogeneous random field are always constant. The covariance function has a number of important properties. They are

1. $C_f(\Delta x, \Delta y) = C_f(-\Delta x, -\Delta y)$ (symmetry)
2. $C_f(\Delta x, \Delta y) \leq C_f(0, 0) = \sigma_f^2$ (decreasing function)
3. $\int_{-\infty}^{\infty} \cdots \int_{-\infty}^{\infty} C_f(x_2 - x_1, y_2 - y_1) \phi(x_1, y_1) \phi(x_2, y_2) dx_1 dx_2 dy_1 dy_2 \geq 0$
(positive definite)

$$4. \quad C_f(\Delta x, \Delta y) \rightarrow 0, \quad |\Delta x|, |\Delta y| \rightarrow \infty$$

When property (4) is valid the random field is said to be ergodic. This enables us to replace the expected operation by an arithmetic averaging operation. Mean, variance and covariance functions are then defined using arithmetic averaging:

$$\begin{aligned} \hat{\mu}_f &= \frac{1}{N} \sum_{i=1}^N f(x_i, y_i) \\ \hat{\sigma}_f^2 &= \frac{1}{N-1} \sum_{i=1}^N [f(x_i, y_i) - \hat{\mu}_f]^2 \\ C_f(\Delta x, \Delta y) &= \frac{1}{N-1} \sum_{i=1}^N [f(x_i + \Delta x, y_i + \Delta y) - \hat{\mu}][f(x_i, y_i) - \hat{\mu}], \quad N \rightarrow \infty \end{aligned} \quad (3.2)$$

When we have two different types of random fields, the relationship between them is expressed in terms of the cross-correlation function defined below:

$$C_{fg}(x_2 - x_1, y_2 - y_1) = E\{(f(x_1, y_1) - \mu_f)(g(x_2, y_2) - \mu_g)\} \quad (3.3)$$

where μ_f and μ_g are means of $f(x, y)$ and $g(x, y)$ fields, respectively. For an ergodic random field, the expected operation in Eq. (3.3) can be replaced by arithmetic averaging:

$$C_{fg}(\Delta x, \Delta y) = \frac{1}{N-1} \sum_{i=1}^N (f(x_i, y_i) - \hat{\mu}_f)(g(x_i + \Delta x, y_i + \Delta y) - \hat{\mu}_g), \quad N \rightarrow \infty \quad (3.4)$$

where $\hat{\mu}_f$ and $\hat{\mu}_g$ are computed via arithmetic averaging, that is

$$\hat{\mu}_f = \frac{1}{N} \sum_{n=1}^N f(x_n, y_n), \quad \hat{\mu}_g = \frac{1}{N} \sum_{n=1}^N g(x_n, y_n), \quad N \rightarrow \infty$$

The cross-correlation function possesses a different set of symmetry relations, namely

$$C_{fg}(\Delta x, \Delta y) = C_{gf}(-\Delta x, -\Delta y)$$

Two random fields are said to be uncorrelated when $C_{fg}(\Delta x, \Delta y) = 0$ for all Δx and Δy . This can happen whenever two fields being correlated do not possess a common generating mechanism. A random field is said to be uncorrelated when its autocorrelation function is a delta function:

$$C_f(\Delta x, \Delta y) = \sigma_f^2 \delta(\Delta x, \Delta y) \quad (3.5)$$

Such a random field, often known as a white noise process, is one whose field measured at two points, however close they may be but not overlapping, is uncorrelated. This is merely a mathematical concept as no real physical field can be purely white. The term ‘coloured noise’ is often used to refer to any noise that is not white. For some processes, the autocorrelation function may become close to zero beyond certain lag, that is

$$C_f(\Delta x, \Delta y) \approx 0 \quad \text{for } \Delta x > \Delta x_0 \text{ and } \Delta y > \Delta y_0$$

The random field is said to possess a correlation distance of $\sqrt{(\Delta x_0^2 + \Delta y_0^2)}$ (for white noise the correlation distance is zero).

A good example of white noise is pseudo-random numbers generated on a computer. They are a uniformly distributed and uncorrelated sequence. A uniformly distributed random sequence can be mapped into a Gaussian random sequence using Box–Mueller transformation [5].

3.2.3. Spectrum and cross-spectrum

We next introduce the power spectrum or simply the spectrum of a random field as a Fourier transform of its autocorrelation function,

$$S_f(u) = \int_{-\infty}^{\infty} C_f(\Delta x) \exp(-ju\Delta x) d\Delta x \quad (3.6)$$

and the cross-spectrum as a Fourier transform of a cross-correlation function

$$S_{fg}(u) = \int_{-\infty}^{\infty} C_{fg}(\Delta x) \exp(-ju\Delta x) d\Delta x \quad (3.7)$$

The spectrum of a two-dimensional stochastic field is similarly defined as the Fourier transform of an autocorrelation function. The spectrum is a positive real function with the following symmetry properties:

$$\begin{aligned} S_f(u, v) &= S_f(-u, -v) \\ S_f(-u, v) &= S_f(u, -v) \end{aligned} \quad (3.8a)$$

The cross-spectrum between two random fields has similar properties

$$\begin{aligned} S_{fg}(u, v) &= S_{gf}^*(-u, -v) \\ S_{fg}(-u, v) &= S_{gf}^*(u, -v) \end{aligned} \quad (3.8b)$$

The property of equality of a spectrum (complex conjugate equality of a cross-spectrum) is illustrated in Figure 3.1. Further,

$$\begin{aligned} \text{var} \{f(x, y)\} &= \frac{1}{4\pi^2} \int \int_{-\infty}^{+\infty} S_f(u, v) du dv \\ S_f(0, 0) &= \int \int_{-\infty}^{+\infty} C_f(\Delta x, \Delta y) d\Delta x d\Delta y \end{aligned} \quad (3.9)$$

3.2.4. Radial and angular spectrum

A two-dimensional spectrum may be expressed in a condensed form as two one-dimensional spectra, viz. a radial spectrum and an angular spectrum. The radial spectrum is defined as

$$R_f(s) = \frac{1}{2\pi} \int_0^{2\pi} S_f(s \cos(\theta), s \sin(\theta)) d\theta \quad (3.10)$$

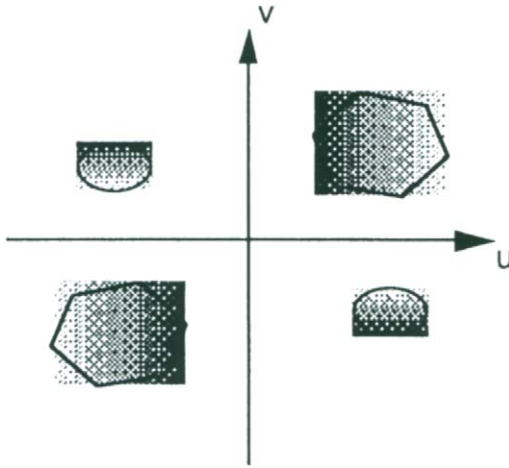


Figure 3.1. The symmetry property of the spectrum and cross-spectrum is illustrated above. The opposite quadrants are symmetric (conjugate symmetric for cross-spectrum) Indeed, it is enough if the spectrum or cross-spectrum is specified in the upper or lower half frequency plane.

where $s = \sqrt{u^2 + v^2}$ and $\theta = \tan^{-1}(v/u)$ are polar coordinates and the angular spectrum is defined as

$$A(\theta) = \frac{1}{\Delta s} \int_{s_0}^{s_0 + \Delta s} S_f[s \cos(\theta), s \sin(\theta)] ds \quad (3.11)$$

where Δs is the radial frequency band starting from s_0 to $s_0 + \Delta s$, over which the averaging is carried out. In order to free the angular spectrum of any radial variation, a normalization with respect to the radial spectrum is applied. Thus, the angular spectrum is expected to bring out the angular variations, if any, of the 2D spectrum of the potential fields. We may normalize the spectrum with respect to the radial spectrum (Eq. (3.10)) and then define the angular spectrum

$$A_{\text{Norm}}(\theta) = \frac{1}{\Delta s} \int_{s_0}^{s_0 + \Delta s} \frac{S_f[s \cos(\theta), s \sin(\theta)]}{R_f(s)} ds \quad (3.12)$$

The numerical computation of the radial and angular spectra requires averaging of the 2D spectrum over concentric rings and wedges as shown in Figure 3.2.

Because of the averaging the radial and angular spectra tend to be smooth

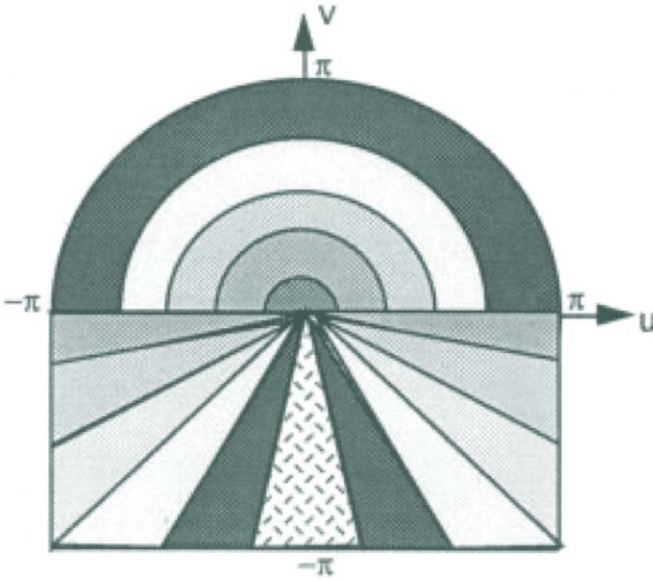


Figure 3.2. A template for computation of the radial spectrum (upper) and the angular spectrum (lower)

functions. The presence of peaks in the angular spectrum gives an indication of linear features in the map. The radial spectrum is a measure of the rate of decay of the spectral power which may represent a deep seated phenomenon such as a deep basement.

3.2.5. Coherence

While the spectrum provides information on how the power is distributed as a function of frequency, the cross-spectrum provides information on the common power that may exist between two fields. In fact we define a quantity called the coherence function which is a measure of the relative common power,

$$\text{Coh}_{fg}(\omega) = \frac{S_{fg}(\omega)}{\sqrt{S_f(\omega)S_g(\omega)}} \quad (3.13)$$

The coherence function is a complex function as the cross-spectrum is a complex function, although the spectrum is a real function. The magnitude of a coherence function lies between 0 and 1. It represents the fraction of power that can be

predicted in field f given the field g , or vice versa [4]. Two fields are said to be non-coherent when the coherence function between the two is zero at least over the frequency band where the signal power is significant. Similarly two fields are coherent when the coherence function magnitude is 1 or in practice close to 1, for example, any two components of the magnetic field are coherent. The presence of noise will decrease the coherence magnitude even though the two fields are theoretically perfectly coherent. In fact in such a case the coherence magnitude becomes a measure of the signal-to-noise ratio (SNR).

3.2.6. Transfer function

Often a physical process can be modelled in terms of a linear system with one or more inputs and one or more outputs. In the context of potential field we have noted in Chapter 2 (p. 56) that the potential field of a layered medium with undulating interfaces can be modelled as a linear system consisting of a layered medium which is 'driven' by an interface (a plane separating the layers is now an undulating surface). The output is the potential field. The input and output are related through a two-dimensional convolution integral,

$$f_{\text{out}}(x, y) = \iint_{-\infty}^{\infty} h(x', y') f_{\text{in}}(x - x', y - y') dx' dy' \quad (3.14)$$

where $h(x, y)$ is known as the impulse response function of the linear system. Taking the Fourier transform on both sides of Eq. (3.14), we obtain

$$F_{\text{out}}(u, v) = H(u, v) F_{\text{in}}(u, v) \quad (3.15a)$$

or

$$H(u, v) = \frac{F_{\text{out}}(u, v)}{F_{\text{in}}(u, v)} \quad (3.15b)$$

where $H(u, v)$ is the Fourier transform of the impulse response function or transfer function of the linear system. When the input and output to a linear system are stationary random functions, the transfer function of a linear system can be expressed in terms of the cross-spectrum and the spectrum [4]

$$H(u, v) = \frac{S_{f_{\text{in}}/f_{\text{out}}}(u, v)}{S_{f_{\text{in}}}(u, v)} \quad (3.16)$$

3.3. Discrete potential fields

The potential fields are naturally continuous functions of space coordinates. They have to be sampled and digitized for the purpose of processing on a digital computer. This brings us to the question of sampling and quantization.

3.3.1. Sampling theorem

A homogeneous random field $f(x)$ is sampled at $x = n\Delta x$, $n = 0, \pm 1, \pm 2, \dots$ where Δx is the sampling interval. The adequacy of sampling is often judged by whether by using the samples we can retrieve the original function with as small an error as possible. Consider the following linear combination:

$$\hat{f}(x) = \sum_{n=-\infty}^{\infty} f(n\Delta x) \frac{\sin \alpha(x - n\Delta x)}{\alpha(x - n\Delta x)} \quad (3.17)$$

where $\alpha = \pi/\Delta x$. A perfect retrieval is achieved when the mean square error is identically zero, that is, $E|f(x) - \hat{f}(x)|^2 = 0$. Indeed this can be achieved under some special conditions [4], namely (i) the spectrum of the field is band limited and (ii) the sampling rate ($= 1/\Delta x$) is at least twice the highest frequency present. The spectrum of the field is said to be band limited when

$$S_f(u) = 0, \quad |u| \geq u_0$$

Let λ_0 be the smallest wavelength corresponding to the highest frequency u_0 ($u_0 = 2\pi/\lambda_0$). Condition (ii) implies that $\Delta x = \lambda_0/2$. A random field with a band limited spectrum is important from the theoretical point of view, although it is doubtful if we ever find a truly band limited process in practice.

3.3.2. Folding of spectrum and aliasing error

For any arbitrary sampling interval the spectrum of the reconstructed function, $\hat{f}(x)$, is related to the spectrum of the original function through the following relation:

$$S_{\hat{f}}(u) = \sum_{n=-\infty}^{\infty} S_f(u + 2n\alpha) \quad (3.18)$$

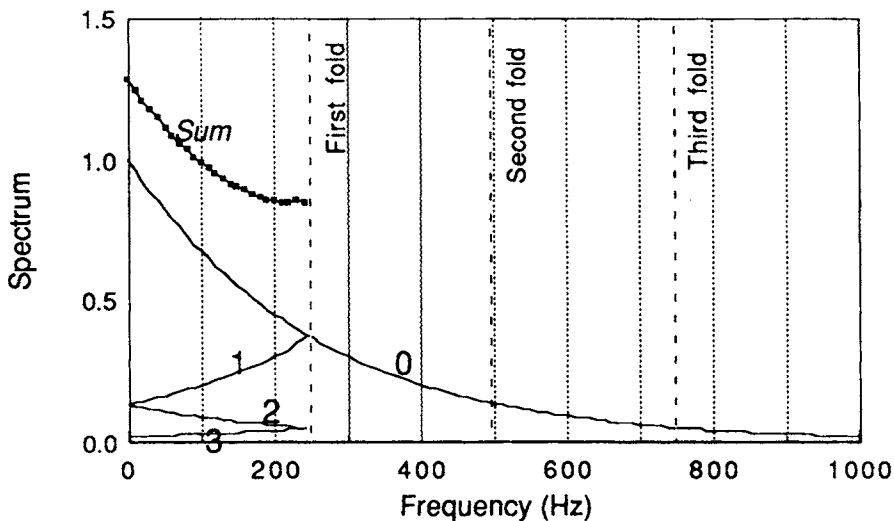


Figure 3.3. Folding of a 1D spectrum. The spectrum of a time series is obtained by successively folding the spectrum of the continuous process as shown above. The first fold is at half the sampling frequency.

It is interesting to picture the mathematical operation involved in Eq. (3.18). Draw a spectral density function on a graph sheet. Mark points on the frequency axis, α angular frequency apart. Fold the frequency axis at the points marked on it. The width of the folded sheet will be 2α . There will be an infinite number of stripes stacked one over the other. Now, transfer all segments of the folded graph onto the base stripe and sum up all segments. The resulting quantity is what appears on the left-hand side of Eq. (3.18). The procedure is demonstrated in Figure 3.3 for an exponentially decaying spectrum.

Naturally, we call $S_f(u)$ the folded spectrum. In general, $S_f(u) \neq S_f(u)$ except when $S_f(u) = 0$ for $|u| > \alpha$. The error introduced by sampling, that is, $(S_f(u) - S_f(u))$ is often called an aliasing error. A random field satisfying the property $S_f(u) = 0$ for $|u| > \alpha$ is called a band limited function. Such a function when sampled with a sampling interval less than or equal to half the smallest wavelength would result in an error free reconstruction, that is to say with no loss of information provided an infinite number of samples are available for interpolation.

A random field in two dimensions can be sampled in more than one way, for example, we may use a square or rectangular grid, polar grid, or hexagonal grid. Such a choice of sampling patterns is not available for a one-dimensional field.

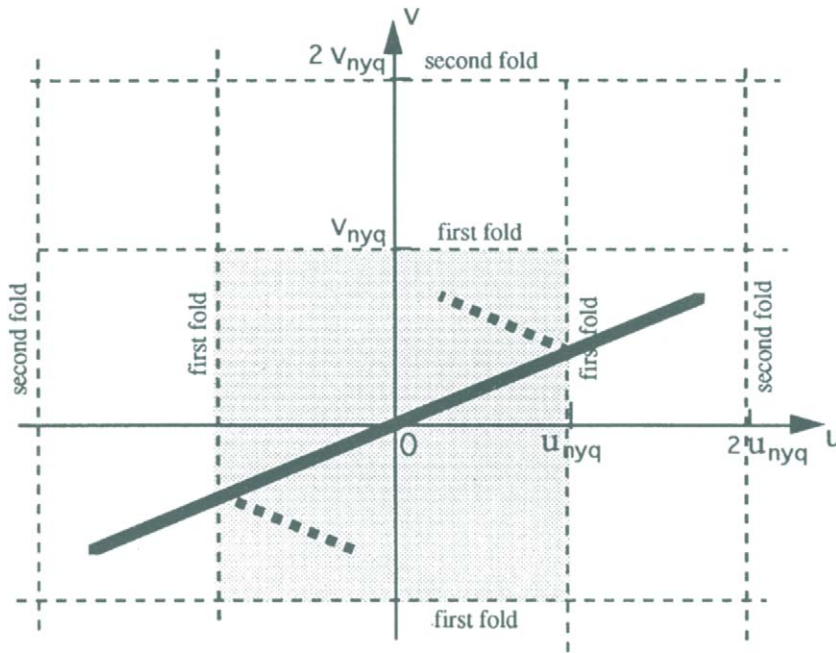


Figure 3.4. Spectral folding in 2D. The spectrum of discrete map data is obtained by folding the spectrum of a continuous map data along the dashed lines, which are spaced at half the sampling frequency. As a result, an interesting situation may arise. A long linear feature in the spectral domain is broken, as shown by the thick dashed line, into three linear features.

However, from practical considerations for implementation of dsp algorithms, a square or rectangular sampling grid is preferred. Also, in this case many results of one-dimensional sampling can be extended to two-dimensional sampling. For example, the folding of spectrum in two dimensions is given by

$$S_f(u, v) = \sum_m \sum_n S_f(u + 2mu_{nyq}, v + 2nv_{nyq}) \quad (3.19)$$

where $u_{nyq} = \pi/\Delta x$ and $v_{nyq} = \pi/\Delta y$. In Figure 3.4 we demonstrate folding of a spectrum associated with two-dimensional sampling. On a graph sheet the frequency axes are now marked u_{nyq} and v_{nyq} angular frequency apart on the u and v axis respectively. The axes are folded on the points marked. There will be infinite number of rectangles stacked one over the other. Now, transfer the spectrum from each rectangle onto the base rectangle and sum up all transferred spectra. The

procedure is demonstrated for a line spectrum, which may be caused by a set of linear features in a map. The folded spectrum shows many lines which may be mistaken as different sets of linear features.

3.3.3. Generalized sampling

Let $f(x,y)$ be a common input to P linear systems whose outputs are measured and sampled. Let $g_k(x,y)$, $k = 1, 2, \dots, P$ be the outputs of P linear systems. Sometimes, it is easy to measure and sample these P outputs, $g_k(x,y)$, $k = 1, 2, \dots, P$ rather than the input, which can then be reconstructed using the samples of the output. In this process, because of the multiple views of the input function, it is possible to reduce the minimum sampling rate required for error free reconstruction of $f(x,y)$ [29]. For example, in aerial surveys one can increase the flight spacing if two transverse derivatives are measured. Let us represent the output of the k th system in the frequency domain

$$g_k(x,y) = \frac{1}{4\pi^2} \int \int_{-\infty}^{+\infty} dF(u,v) H_k(u,v) \exp(j(ux + vy)) \, dx \, dy, \quad k = 1, 2, \dots, P \quad (3.20)$$

where $H_k(u,v)$ is the transfer function of the k th system. We assume that the spectrum of the input process is band limited to $[\pm B_0, \pm B_0]$. Let us sample the output function at intervals Δx and Δy which are related to the maximum frequency as

$$\Delta x = \Delta y = \nu \frac{\pi}{B_0}$$

where ν is a constant yet to be determined ($\nu = 1$ for Nyquist rate sampling of $f(x,y)$). Let $a_k(x - m\Delta x, y - n\Delta y)$, $k = 1, 2, \dots, P$ be a set of interpolating functions defined as

$$\hat{f}(x,y) = \sum_k \sum_m \sum_n g_k(m\Delta x, n\Delta y) a_k(x - m\Delta x, y - n\Delta y) \quad (3.21)$$

We wish to estimate the interpolating functions and the sampling intervals such that the mean square error between $\hat{f}(x,y)$ and $f(x,y)$ is minimum. The mean

square error is given by

$$E\{|f(x, y) - \hat{f}(x, y)|^2\} = C_f(0, 0) + C_{\hat{f}}(0, 0) - 2C_{f\hat{f}}(0, 0)$$

where

$$C_f(0, 0) = E\{f^2(x, y)\}$$

$$C_{\hat{f}}(0, 0) = \sum_m \dots \sum_l C_{g_k g_l}((m - m')\Delta x, (n - n')\Delta y) a_k(x - m\Delta x, y - n\Delta y) \\ \times a_l(x - m'\Delta x, y - n'\Delta y)$$

and

$$C_{f\hat{f}}(0, 0) = \sum_m \sum_n \sum_k C_{fg_k}(x - m\Delta x, y - n\Delta y) a_k(x - m\Delta x, y - n\Delta y)$$

Further, we have

$$C_{g_k g_l}((m - m')\Delta x, (n - n')\Delta y) \\ = \frac{1}{4\pi^2} \int \int_{-B_0}^{+B_0} S_f(u, v) H_k(u, v) H_l^*(u, v) \exp[j(u(m - m')\Delta x + v(n - n')\Delta y)] du dv \\ C_{fg_k}(x - m\Delta x, y - n\Delta y) \\ = \frac{1}{4\pi^2} \int \int_{-B_0}^{+B_0} S_f(u, v) H_k^*(u, v) \exp[j(u(x - m\Delta x) + v(y - n\Delta y))] du dv \quad (3.22)$$

Define,

$$A_k(u, x; v, y) = \sum_m \sum_n a_k(x - m\Delta x, y - n\Delta y) \exp(-j(um\Delta x + vn\Delta y))$$

Using the above quantities we can rewrite the mean square difference as follows:

$$\begin{aligned}
& E\{|f(x, y) - \hat{f}(x, y)|^2\} \\
&= \frac{1}{4\pi^2} \int \int_{-B_0}^{+B_0} S_f(u, v) \left[1 + \left| \sum_k A_k(u, x; v, y) H_k(u, v) \right|^2 \right. \\
&\quad \left. - 2 \exp(j(ux + vy)) \sum_k A_k(u, x; v, y) H_k^*(u, v) \right] du dv
\end{aligned}$$

For the mean square error to become zero, that is, for perfect reconstruction the quantity inside the square brackets must be zero (since $S_f(u, v) > 0$). For this to be true we must have

$$\sum_k H_k^*(u, v) A_k(u, x; v, y) = \exp(-j(ux + vy)) \quad (3.23)$$

for all (x, y) and $(|u|, |v| \leq B_0)$. Note that $A_k(u, x; v, y)$ is periodic in u and v with a period of $[\pm B_0/\nu, \pm B_0/\nu]$. Let us divide the frequency range $[\pm B_0, \pm B_0]$ into ν^2 equal divisions (square tiles as shown in Figure 3.5),

$$\left\{ -B_0 \text{ to } -B_0 + \frac{2B_0}{\nu}, -B_0 \text{ to } -B_0 + \frac{2B_0}{\nu} \right\} \quad (\text{tile \#1})$$

$$\left\{ -B_0 \text{ to } -B_0 + \frac{2B_0}{\nu}, -B_0 + \frac{2B_0}{\nu} \text{ to } -B_0 + \frac{4B_0}{\nu} \right\} \quad (\text{tile \#2})$$

$$\left\{ -B_0 + \frac{iB_0}{\nu} \text{ to } -B_0 + \frac{(i+1)B_0}{\nu}, -B_0 + \frac{jB_0}{\nu} \text{ to } -B_0 + \frac{(j+1)B_0}{\nu} \right\} \quad (\text{tile \#(i,j)})$$

Since $A_k(u, x; v, y)$ repeats over these tiles, Eq. (3.23) gives rise to a system of ν^2 equations,

$$\sum_k H_k^*(\tilde{u}, \tilde{v}) A_k(\tilde{u}, x; \tilde{v}, y) = 1$$

$$\sum_k H_k^*\left(\tilde{u} + \frac{2B_0}{\nu}, \tilde{v}\right) A_k(\tilde{u}, x; \tilde{v}, y) = \exp\left(-j \frac{2B_0}{\nu} x\right)$$

$$\sum_k H_k^*(\tilde{u}, \tilde{v} + \frac{2B_0}{\nu}) A_k(\tilde{u}, x; \tilde{v}, y) = \exp\left(-j \frac{2B_0}{\nu} y\right)$$

$$\begin{aligned} \sum_k H_k^*(\tilde{u} + (\nu - 1) \frac{2B_0}{\nu}, \tilde{v} + (\nu - 1) \frac{2B_0}{\nu}) A_k(\tilde{u}, x; \tilde{v}, y) \\ = \exp\left[-j \left((\nu - 1) \frac{2B_0}{\nu} x + (\nu - 1) \frac{2B_0}{\nu} y\right)\right] \end{aligned} \quad (3.24)$$

where \tilde{u} and \tilde{v} are now limited to the first tile (see Figure 3.5). A factor $\exp(j(\tilde{u}x + \tilde{v}y))$ has been absorbed into $A_k(\tilde{u}, x; \tilde{v}, y)$. There are ν^2 equations in Eq. (3.24) which may be solved for $A_k(\tilde{u}, x; \tilde{v}, y)$, $k = 1, 2, \dots, P$. For a unique solution we must have $\nu = \sqrt{P}$. Thus, we have a gain of \sqrt{P} in terms of reduced sampling rate. In the context of a precision aeromagnetic survey the

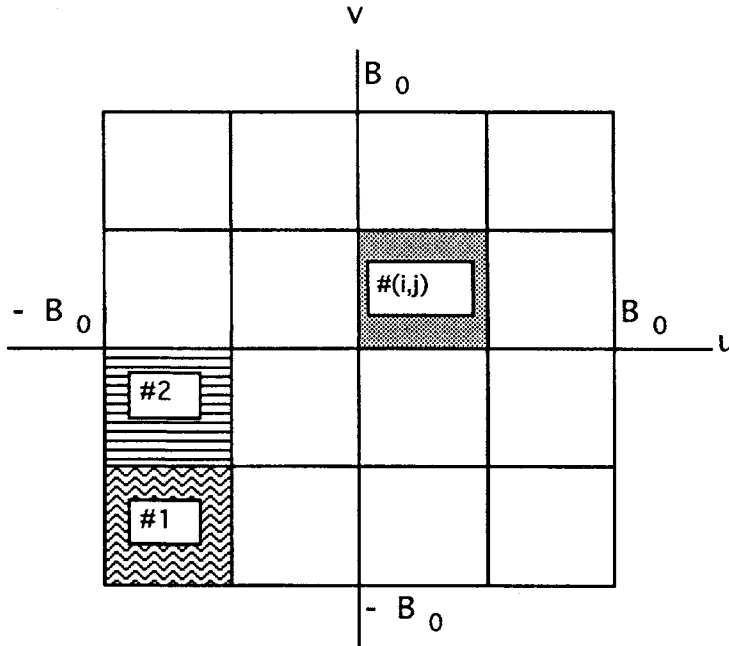


Figure 3.5. The signal band is divided into ν^2 tiles each of size $(2B_0/\nu) \times (2B_0/\nu)$. Here $\nu = 4$.

major limitation comes from the diurnal and rapid variations of the earth's field (see Chapter 1 for discussion). This problem may be overcome by measuring the spatial derivatives instead of the field itself. If the derivatives are measured across the flight direction (transverse derivatives) we can at the same time reduce the sampling rate and thus increase the line spacing. If we were to measure two horizontal derivatives using, say, three magnetometers, it is possible to double the line spacing. The required interpolation filters are derived in Example 3.1.

Example 3.1

Let us assume that two horizontal derivatives (first and second derivatives) across the direction of flight are measured with the help of three magnetometers (two in the wing tips and one in the tail). This specifies $H_k(u)$ in Eq. (3.20)

$$g_k(x, y) = \frac{1}{4\pi^2} \int \int_{-\infty}^{+\infty} dF(u, v) H_k(u) \exp(j(ux + vy)) dx dy, \quad k = 1, 2$$

as

$$H_1(u) = ju, \quad H_2(u) = -u^2$$

where we have assumed that the flight direction is along y . The sampling intervals in the x and y directions are $\Delta x = \pi/B_0$ and $\Delta y = \pi/B_0$. Now the interpolation filter $A_k(u, x; v, y)$ will be periodic over rectangular tiles as shown in Figure 3.6.

Eq. (3.24) reduces to a system of 2×2 equations,

$$H_1^*(\tilde{u})A_1(\tilde{u}, x; v, y) + H_2^*(\tilde{u})A_2(\tilde{u}, x; v, y) = 1$$

$$H_1^*(\tilde{u} + B_0)A_1(\tilde{u}, x; v, y) + H_2^*(\tilde{u} + B_0)A_2(\tilde{u}, x; v, y) = \exp(-jB_0x)$$

where $-B_0 \leq \tilde{u} \leq 0$ and $-B_0 \leq v \leq B_0$ and an additional factor, $\exp(j\tilde{u}x)$, is absorbed in the interpolation filters. The solution of above system of equations is quite straightforward:

$$A_1(\tilde{u}, x; v, y) = \frac{-(\tilde{u} + B_0)^2 + \tilde{u}^2 \exp(-jB_0x)}{j\tilde{u}B_0(\tilde{u} + B_0)}$$

$$A_2(\tilde{u}, x; v, y) = \frac{(\tilde{u} + B_0) - \tilde{u} \exp(-jB_0x)}{\tilde{u}B_0(\tilde{u} + B_0)}$$

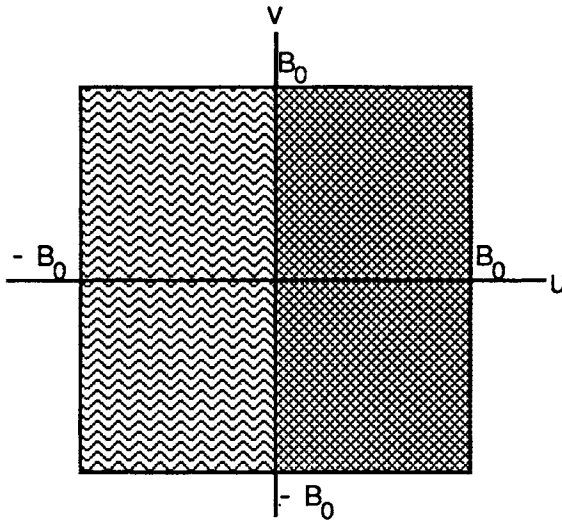


Fig.3.6. The signal band is divided into two rectangular tiles each of size $B_0 \times 2B_0$.

It may be observed that the transfer function of the interpolation filters are singular at $\tilde{u} = 0$ and $\tilde{u} = -B_0$.

3.3.4. Quantization errors

Along with sampling we must account for quantization. Since numbers in computer memory are represented by a finite number of bits there will always be some error in the representation. Also, the sensors used for field measurements and the associated electronic circuitry impose a finite precision on the measured data, for example, in a typical aerial survey the magnetic field can be measured within an error of $\pm 0.5\gamma$ [6]. The number of bits required to represent a measured quantity is dictated by the measurement precision and the dynamic range such that the error due to finite word length representation is matched to the measurement precision. The error due to finite word length is often known as the quantization error. Let $f_q(x)$ be the quantized field and $\varepsilon(x)$ be the quantization error. Then,

$$f_q(x) = f(x) + \varepsilon(x)$$

where $\varepsilon(x)$ is the quantization error, which is often modelled as uniformly dis-

tributed and uncorrelated random noise. As an illustration of the quantization effect, an analog sinusoid, its quantized version and the resulting error are shown in Figure 3.7a. The spectrum of the quantized signal is given by

$$S_{f_q}(u) = S_f(u) + \sigma_\varepsilon^2 \quad (3.25)$$

where σ_ε^2 is the variance of the quantization noise. From Eq. (3.25) it is clear that the quantization noise power can submerge the weak signal peaks if the quantization is too coarse. Let the quantization step be Δ , then, assuming ε is uniformly distributed in the range $\pm\Delta/2$ the quantization noise power σ_ε^2 is equal to $\Delta^2/12$. The effect of quantization on a simple waveform such as a sinusoid is demonstrated in Example 3.2.

Example 3.2

A pure sinusoidal signal, $\sin(0.1t)$, is sampled and then quantized to eight levels (each level of size $\Delta = 0.125$). Here t stands for time. The continuous waveform and quantized waveform are shown in Figure 3.7a and the difference between the two is shown in Figure 3.7b. Notice the noise like appearance of the difference waveform. For this reason the difference waveform is modelled as white noise particularly when the quantization is fine.

3.4. Estimation of power spectrum

The modern methods of spectrum estimation are closely linked with the underlying model of the time series [4]. Many of the models used in the analysis of time series have not found usefulness in the geophysical potential fields. Only the very basic model where the potential field is expressed as a linear combination of randomly distributed sources (equivalent to the moving average (MA) model of time series) has been used. The spectrum estimation approach is therefore based on classical methods, such as those of Blackman and Tukey and Welch [4]. We shall emphasize the Welch method which uses the fast Fourier transform algorithm to compute the discrete Fourier transform of large map data.

3.4.1. Discrete Fourier transform (dft)

The Fourier transform of a two-dimensional function is defined as follows:

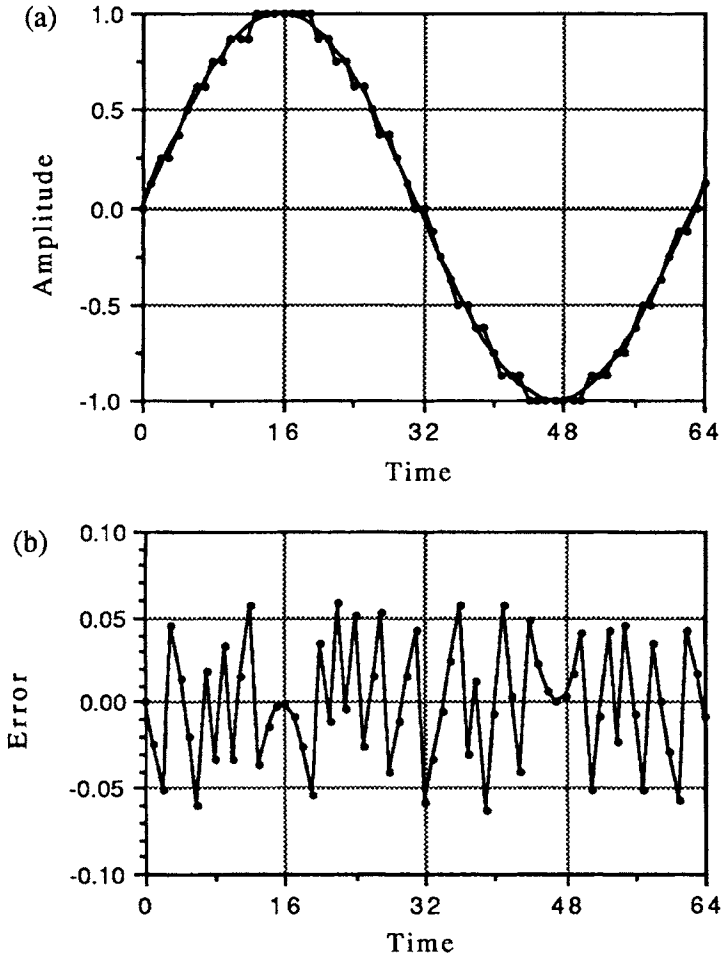


Figure 3.7. A sinusoid $\sin(0.1t)$ is quantized to eight levels (each level of size $\Delta = 0.125$). The quantized and original waveforms are shown in (a) and the difference (error) is shown in (b).

$$F(u, v) = \int \int_{-\infty}^{+\infty} f(x, y) \exp(-j(ux + vy)) dx dy \quad (3.26)$$

Analogously the discrete Fourier transform (dft) is defined as follows:

$$F_d(k, l) = \sum_{m=0}^{M-1} \sum_{n=0}^{N-1} f(m, n) \exp\{-j2\pi[(mk/M) + (nl/N)]\}$$

$$0 \leq k \leq M - 1 \quad \text{and} \quad 0 \leq l \leq N - 1 \quad (3.27)$$

The discrete Fourier transform $F_d(k, l)$ is quite analogous to the continuous Fourier transform $F(u, v)$. The analogy is better brought out if we identify the indices k and l with the frequencies u and v respectively. Indeed the relationship is given by

$$u = \frac{2\pi k}{M} \quad \text{and} \quad v = \frac{2\pi l}{N}$$

For this reason the indices k and l are often called frequency numbers. It may appear that Eq. (3.27) is a discrete version of Eq. (3.26). This, however, is not necessary as the discrete Fourier transform can stand on its own. For example it has its own inverse transform defined as follows:

$$f(m, n) = \frac{1}{MN} \sum_{k=0}^{M-1} \sum_{l=0}^{N-1} F_d(k, l) \exp\{+j2\pi[(mk/M) + (nl/N)]\}$$

$$0 \leq m \leq M - 1 \quad \text{and} \quad 0 \leq n \leq N - 1 \quad (3.28)$$

When the data length is large, ideally infinite, Eq. (3.27) may be written as

$$F_d(u, v) = \sum_{-\infty}^{\infty} \sum_{-\infty}^{\infty} f(m, n) \exp[-j(um + vn)] \quad (3.29)$$

and the corresponding inverse transform may be written as

$$f(m, n) = \frac{1}{4\pi^2} \int_{-\pi}^{\pi} \int_{-\pi}^{\pi} F_d(u, v) \exp[j(um + vn)] du dv \quad (3.30)$$

Let us call $F_d(u, v)$ as ideal dft obtained from an infinite data matrix.

We now introduce a windowed dft, that is, a dft of a data matrix which has been tapered by a suitable function called a window function. Let $f_w(m, n) = f(m, n)w(m, n)$ where $w(m, n)$ is the window function having the following property:

$$w(m, n) = 0 \text{ for } m \notin 0, \dots, M-1$$

$$n \notin 0, \dots, N-1$$

Let us now demonstrate the basic role of a window. For this we compute the dft of a windowed data matrix.

$$\begin{aligned}
 F_d(k, l) &= \sum_{m=0}^{M-1} \sum_{n=0}^{N-1} f_w(m, n) \exp\{-j2\pi[(mk/M) + (nl/N)]\} \\
 &= \sum_{-\infty}^{\infty} \sum_{-\infty}^{\infty} f(m, n) w(m, n) \exp\{-j2\pi[(mk/M) + (nl/N)]\} \\
 &= \frac{1}{4\pi^2} \int_{-\pi}^{\pi} \int_{-\pi}^{\pi} F_d(u, v) W\left(\frac{2\pi k}{M} - u, \frac{2\pi l}{N} - v\right) du dv \\
 &= F_w(k, l), \quad 0 \leq k \leq M-1 \quad \text{and} \quad 0 \leq l \leq N-1
 \end{aligned} \tag{3.31}$$

where $W(u, v)$ is the dft of the window function and $F_d(k, l)$ is the windowed dft. From Eq. (3.31) it is clear that the windowed dft is a convolution between the ideal dft of infinite data matrix and the dft of the window function. When there is no deliberate taper applied to the data, the window function is simply unity, that is

$$w(m, n) = 1 \text{ for } m \in 0, \dots, M-1$$

$$n \in 0, \dots, N-1$$

and zero outside. We call this a default window. The dft of the default window is given by

$$w(u, v) = \text{sinc}\left(\frac{1}{2}uM\right) \text{sinc}\left(\frac{1}{2}vN\right) \exp\left[-j\left(\frac{1}{2}uM + \frac{1}{2}vN\right)\right]$$

where

$$\text{sinc}(x) = \frac{\sin(x)}{x}$$

It is important to understand the role of a window function. Firstly, note that the windowed dft does not have a one to one relationship with the ideal dft. Because

of the convolution operation the sharp peaks in the ideal dft, if any, are smudged. Further there is some amount of power leakage resulting in the appearance of spurious peaks. This effect is demonstrated in Figure 3.8. The spectrum of a pure sinusoid is a delta function as shown in Figure 3.8a. We take just 16 samples from this sinusoid and compute its spectrum and the result is as shown in Figure 3.8b.

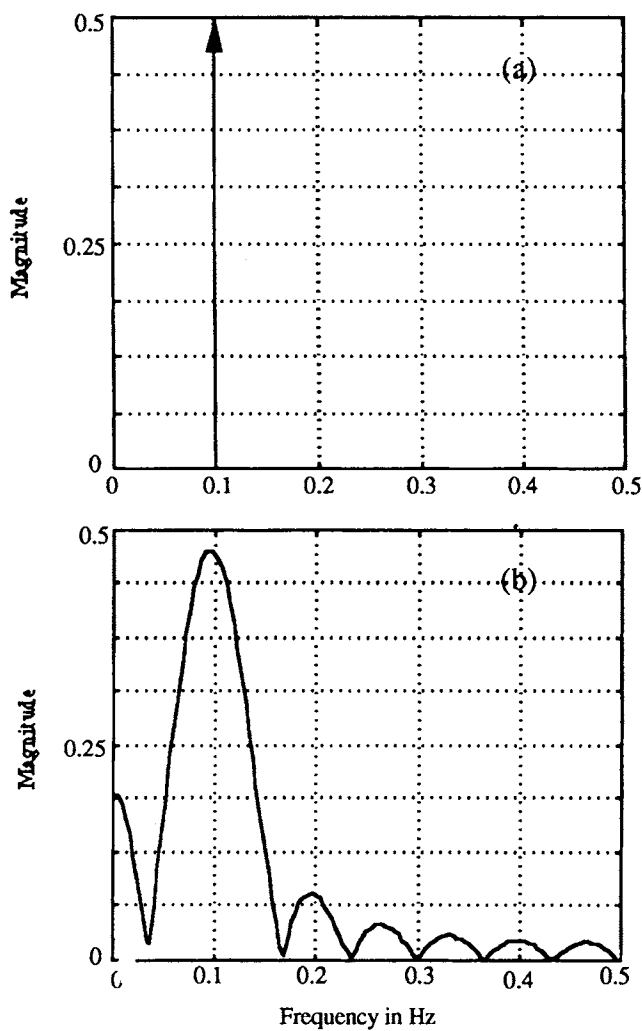


Figure 3.8. The effect of a default window (rectangular window) on the spectrum of a unit magnitude sinusoid. (a) Spectrum of infinite length sinusoid and (b) spectrum of 16 samples of sinusoid (2 samples/period).

The sharp peak corresponding to the sinusoid has now become a broad peak. Further, we notice many minor peaks created by the leakage of power through the side lobes of the dft of the window. Both smudging and creation of spurious peaks can be controlled by appropriate design of the window function. The default window has the least smudging effect but the worst spurious peak phenomenon. Design of good windows is beyond the scope of this work. The readers are encouraged to refer to current books and papers, for example [4,7,8].

3.4.2. Fast Fourier transform (FFT)

The Fourier transform of discrete data turns out to be one of the basic steps in a data processing exercise. Several fast algorithms are available for the evaluation of the discrete Fourier transform (dft). There are different variations of the now famous fast Fourier transform (FFT) algorithm, first invented by Runge and Konig [9] and rediscovered by Tukey and Cooley [10]. We briefly describe the basic algorithm emphasizing how the increase in the speed of computation is achieved. Evaluation of dft Eq. (3.27) in the normal course would require N^2 complex operations (one complex operation consists of one addition and one multiplication). We now demonstrate that by a simple trick of splitting the data into two halves the number of operations can be reduced to a little over $N^2/2$. We split the given sequence into two equal length sequences as follows:

$$f_1(n_1) = f(2n_1)$$

$$f_2(n_1) = f(2n_1 + 1), \quad n_1 = 0, 1, \dots, \frac{1}{2}(N - 1)$$

$f_1(n_1)$ contains all even indexed data points and $f_2(n_1)$ contains all odd indexed data points. Now consider the dft of $f(n)$ in terms of the dft of $f_1(n_1)$ and $f_2(n_1)$.

$$\begin{aligned} F(k) &= \sum_{n=0}^{N-1} f(n) \exp \left[-j \left(\frac{2\pi}{N} \right) nk \right] \\ &= \sum_{n=0}^{N/2-1} f(2n) \exp \left[-j \left(\frac{2\pi}{N} \right) 2nk \right] \\ &\quad + \sum_{n=0}^{N/2-1} f(2n+1) \exp \left[-j \left(\frac{2\pi}{N} \right) (2n+1)k \right] \end{aligned}$$

$$\begin{aligned}
&= \sum_{n=0}^{N/2-1} f_1(n) \exp \left[-j \left(\frac{2\pi}{N/2} \right) nk \right] \\
&\quad + \sum_{n=0}^{N/2-1} f_2(n) \exp \left[-j \left(\frac{2\pi}{N/2} \right) nk \right] \exp \left[-j \left(\frac{2\pi}{N} \right) k \right] \\
&= F_1(k) + F_2(k) \exp \left[-j \left(\frac{2\pi}{N} \right) k \right] \quad \text{for } k = 0, 1, \dots, N/2 - 1 \\
&= F_1(k) + F_2(k) \exp \left[-j \left(\frac{2\pi}{N} \right) k \right] \quad \text{for } k = N/2, N/2 + 1, \dots, N - 1
\end{aligned} \tag{3.32}$$

The above equation shows how to combine the dft of two half sequences into the dft of the full sequence. This is often known as a doubling algorithm which is illustrated in Figure 3.9 where the signal flow diagram is often referred to as a butterfly.

Let us now count the number of complex operations required to evaluate the dft using Eq. (3.32). The two half sequences would require $N^2/4$ complex operations each; in addition we would require N operations to evaluate Eq. (3.32). Thus we now need $N^2/2 + N$ operations compared to N^2 operations using straightforward evaluation of Eq. (3.27). Nearly a 50% reduction could be achieved by a simple trick of splitting the full sequence into two half sequences. It is clear how

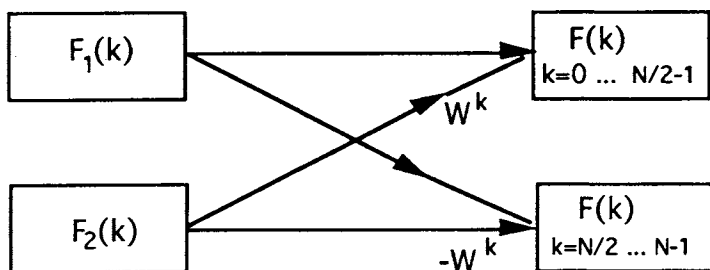


Figure 3.9. Doubling algorithm where the Fourier transform of two half sequences are combined into one sequence. The multiplicative factor is known as the twiddle factor, $W^k = \exp \left[-j \left(\frac{2\pi}{N} \right) k \right]$.

one can exploit the above property in a repeated manner to significantly reduce the number of operations. It turns out that a sequence of N points requires just about $N \log_2 N$ operations (N is equal to a power of 2). The fast Fourier transform algorithm basically consists of several interconnected butterflies as shown in Figure 3.9.

3.4.3. 2D discrete Fourier transform

The discrete Fourier transform of a two-dimensional discrete data can be obtained by repeated application of dft first along rows and then columns. Each row is replaced by its dft and then each column is replaced by dft. The number of operations required would be $N^2 \log_2 N$ while the direct evaluation would require N^4 operations. It may be noted that this popular approach requires matrix transposition, an operation that requires a fair amount of computation if the data are residing on a sequential storage device such as disc or magnetic tape. However, efficient methods do exist to carry out the matrix transposition operation [11]. The matrix transposition can be completely avoided if the dft operation is carried out along both directions. In addition, there is a further reduction in the computational load. We briefly outline the so-called direct method, also known as the vector radix method. This can be significant in reducing the heavy computational load in Fourier transforming large geophysical maps.

Let us introduce the following transformations in Eq. (3.27):

$$m = 2m_1 + m_0, \quad n = 2n_1 + n_0$$

and

$$k = M_1 k_1 + k_0, \quad l = N_1 l_1 + l_0$$

where

$$M_1 = \frac{M}{2}, \quad N_1 = \frac{N}{2}$$

$$m_0 = 0, 1, \quad n_0 = 0, 1$$

$$m_1 = 0, 1, \dots, M_1 - 1, \quad n_1 = 0, 1, \dots, N_1 - 1$$

$$k_0 = 0, 1, \dots, M_1 - 1, \quad l_0 = 0, 1, \dots, N_1 - 1$$

$$k_1 = 0, 1, \quad l_1 = 0, 1$$

We obtain a set of equation analogous to Eq. (3.32), the doubling algorithm in 1-D discrete Fourier transformation.

$$\begin{aligned}
F(k, l)|_{k_1, l_1=0} &= F_1(k_0, l_0) + F_2(k_0, l_0) \exp \left[-j \left(\frac{2\pi}{N} \right) l_0 \right] \\
&\quad + F_3(k_0, l_0) \exp \left[-j \left(\frac{2\pi}{M} \right) k_0 \right] + F_4(k_0, l_0) \exp \left[-j 2\pi \left(\frac{k_0}{M} + \frac{l_0}{N} \right) \right] \\
F(k, l)|_{k_1=1, l_1=0} &= F_1(k_0, l_0) + F_2(k_0, l_0) \exp \left[-j \left(\frac{2\pi}{N} \right) l_0 \right] \\
&\quad - F_3(k_0, l_0) \exp \left[-j \left(\frac{2\pi}{M} \right) k_0 \right] - F_4(k_0, l_0) \exp \left[-j 2\pi \left(\frac{k_0}{M} + \frac{l_0}{N} \right) \right] \\
F(k, l)|_{k_1=0, l_1=1} &= F_1(k_0, l_0) - F_2(k_0, l_0) \exp \left[-j \left(\frac{2\pi}{N} \right) l_0 \right] \\
&\quad + F_3(k_0, l_0) \exp \left[-j \left(\frac{2\pi}{M} \right) k_0 \right] - F_4(k_0, l_0) \exp \left[-j 2\pi \left(\frac{k_0}{M} + \frac{l_0}{N} \right) \right] \\
\text{and} \\
F(k, l)|_{k_1=1, l_1=1} &= F_1(k_0, l_0) - F_2(k_0, l_0) \exp \left[-j \left(\frac{2\pi}{N} \right) l_0 \right] \\
&\quad - F_3(k_0, l_0) \exp \left[-j \left(\frac{2\pi}{M} \right) k_0 \right] + F_4(k_0, l_0) \exp \left[-j 2\pi \left(\frac{k_0}{M} + \frac{l_0}{N} \right) \right]
\end{aligned} \tag{3.33}$$

where

$$F_1(k_0, l_0) = \text{DFT}\{f((0, m_1), (0, n_1))\}, \quad \text{Even columns and even rows}$$

$$F_2(k_0, l_0) = \text{DFT}\{f((0, m_1), (1, n_1))\}, \quad \text{Even columns and odd rows}$$

$$F_3(k_0, l_0) = \text{DFT}\{f((1, m_1), (0, n_1))\}, \quad \text{Odd columns and even rows}$$

$$F_4(k_0, l_0) = \text{DFT}\{f((1, m_1), (1, n_1))\}, \quad \text{Odd columns and odd rows}$$

Eq. (3.33) is a doubling algorithm in direct 2D-dft as Eq. (3.32) is in 1D-dft. It

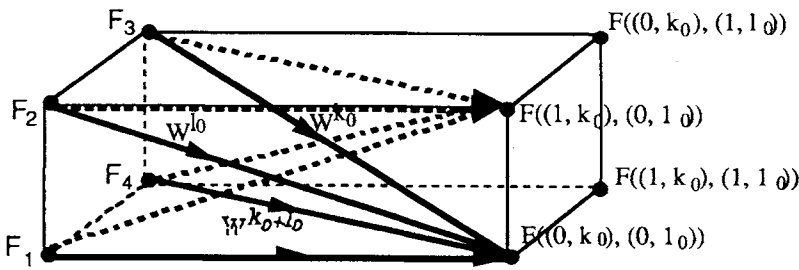


Figure 3.10. Signal flow diagram of the doubling algorithm (Vector butterfly) in direct 2D-dft.

combines dft of four quarter matrices into a dft of full data matrix. The signal flow diagram, known as a vector butterfly, is shown in Figure 3.10.

Note that, for the sake of clarity, only one half of the butterfly is shown. By repeated application of the doubling algorithm we can obtain 2D-dft recursively, starting with an elementary matrix of 1×1 whose dft is simply itself. The doubling algorithm requires three complex operations (i.e. three complex additions and three multiplications). There are $\log N$ recursive stages and in each stage the doubling algorithm is executed N^2 times; thus, we have $3N^2 \log N$ complex operations. But in the usual row-column approach we have as pointed out earlier $N^2 \log N$ complex operations. It would therefore seem that the direct method would be slower than the row-column method. However, this is not true if we remove the redundant operations in the doubling algorithm. Note that out of 12 complex multiplications (in all four cases) only three multiplications are different and the rest are simple repetitions. As a result the count of complex multiplications reduces to $3/4 N^2 \log N$. Thus, the direct method becomes faster than the row-column method by about 25%. The drawback of the direct method is that the entire data matrix must reside inside the computer memory. The direct method was first suggested by Rivard [12]. A modern treatment of the discrete Fourier transform and the FFT algorithm may be found in Ref. [13]

3.4.4. Properties of dft coefficients

The 2D-dft coefficients possess several useful properties which we quote without proof. These are straightforward extensions of 1-D dft coefficients [4].

1. $F(k, l) = F(k + M, l + N)$ (periodicity)
2. $F(-k, -l) = F(M - k, N - l)$
3. $F(-k, l) = F(M - k, l)$
4. $F(k, -l) = F(k, N - l)$ (symmetry) (3.34a)

For real data, further symmetries in the dft coefficients exist, namely

5. $F(k, l) = F^*(-k, -l)$
6. $F(-k, l) = F^*(k, -l)$
7. $F(k, -l) = F^*(-k, l)$ (symmetry for real data) (3.34b)

As a result of the above symmetry properties, the 2-D dft coefficients of a square data matrix are arranged in a manner illustrated in Figure 3.11. The zero frequency dft coefficient is located at $k = l = 0$. The dft coefficients for negative frequency numbers are located in II, III, IV quadrants as shown.

A $M \times N$ data matrix will give rise to $M \times N$ dft coefficients. For the purpose

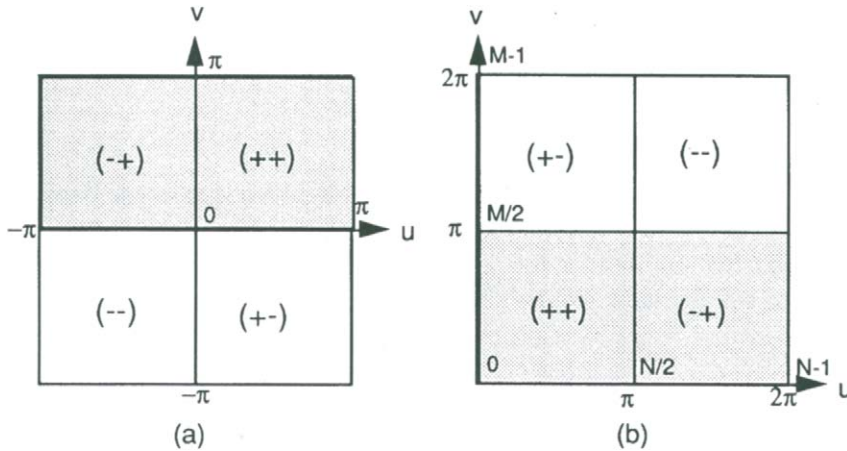


Figure 3.11. (a) Fourier transform of an infinite data matrix is periodic. The principal period is a square with its centre of coordinates at the centre of the square. (b) In the discrete Fourier transform of a square data matrix (which is replicated over the entire plane) the four quadrants of the principle period in (a) are rearranged as shown. This arrangement is often known as dft symmetry.

of graphical illustration a small size coefficient matrix is not appropriate as it does not give a smooth appearance. Often it is necessary to interpolate between the coefficients. This is best achieved by padding a large number of zeros to the data matrix before computing its dft. The output contains as many coefficients as the size of the input matrix which has been expanded by padding zeros. We show here that the resulting extra dft coefficients are the result of interpolation. Let a data matrix $f(m,n)$, $m = 0,1,\dots,M - 1$; $n = 0,1,\dots,N - 1$ be expanded by padding zeros to matrix of size $pM \times pN$ where p is an integer. Some of the possible ways of padding zeros are shown in Figure 3.12.

We consider the first type as it leads to a simpler mathematical expression. The dft of the expanded matrix is given by

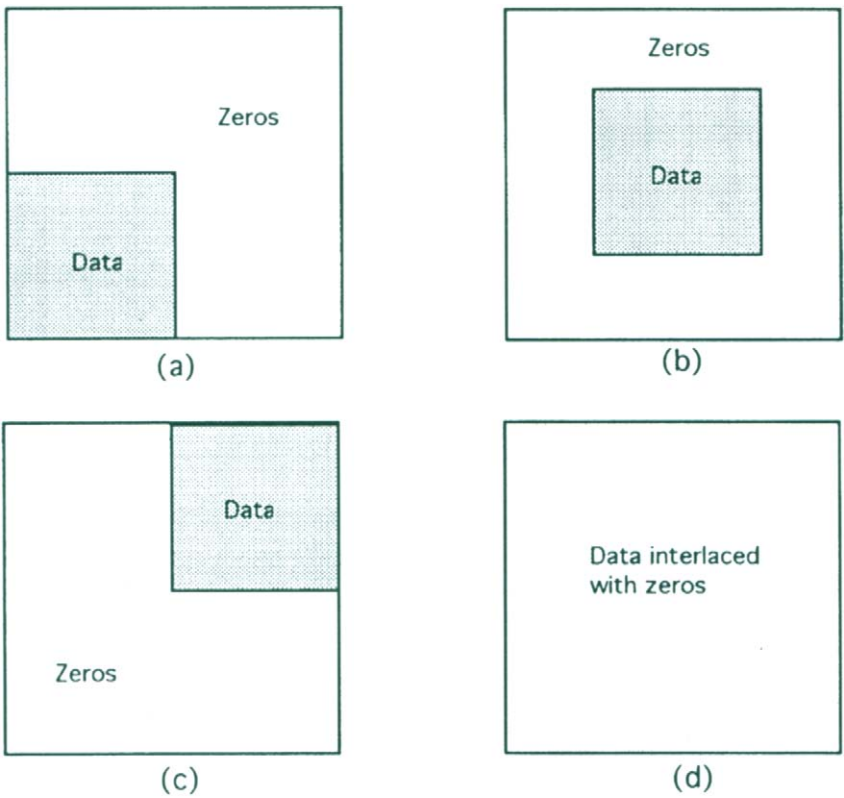


Figure 3.12. For the purpose of interpolation, the data matrix is expanded by padding zeros. Some of the possible methods of padding zeros are shown above. In (d) the data are interlaced with zeros. This method is useful when the data are required to be interpolated.

$$\begin{aligned}
F_p(k, l) &= \sum_{m=0}^{pM-1} \sum_{n=0}^{pN-1} f_p(m, n) \exp \left\{ -j \left[\left(\frac{2\pi}{pM} \right) km + \left(\frac{2\pi}{pN} \right) ln \right] \right\} \\
&= \sum_{m=0}^{M-1} \sum_{n=0}^{N-1} f(m, n) \exp \left\{ -j \left[\left(\frac{2\pi}{pM} \right) km + \left(\frac{2\pi}{pN} \right) ln \right] \right\} \quad (3.35a)
\end{aligned}$$

where

$$\begin{aligned}
f_p(m, n) &= f(m, n) \quad \text{when } 0 \leq m \leq M-1 \text{ and } 0 \leq n \leq N-1 \\
&= 0.0 \quad \text{when } M \leq m \leq pM-1 \text{ and } N \leq n \leq pN-1
\end{aligned}$$

Let $k = pk_1 + k_0$ and $l = pl_1 + l_0$ where $k_1 = 0, 1, \dots, M-1$, $k_0 = 0, 1, \dots, p-1$, $l_1 = 0, 1, \dots, N-1$ and $l_0 = 0, 1, \dots, p-1$. Making the above substitutions into Eq. (3.35a), we obtain

$$\begin{aligned}
F_p(k, l) &= \sum_{m=0}^{M-1} \sum_{n=0}^{N-1} f(m, n) \exp \left\{ -j2\pi \left[\left(\frac{k_1}{M} + \frac{k_0}{pM} \right) m + \left(\frac{l_1}{N} + \frac{l_0}{pN} \right) n \right] \right\} \\
&= \sum_{m=0}^{M-1} \sum_{n=0}^{N-1} \left\{ f(m, n) \exp \left[-j2\pi \left(\frac{k_0 m}{pM} + \frac{l_0 n}{pN} \right) \right] \right\} \exp \left[-j2\pi \left(\frac{k_1 m}{M} + \frac{l_1 n}{N} \right) \right]
\end{aligned}$$

which may be simplified to

$$\begin{aligned}
F_p(k, l) &= F(k_1, l_1) \times \frac{\sin \left[\pi \left(\frac{k_0}{p} + k_1 \right) \right]}{\sin \left[\frac{\pi}{M} \left(\frac{k_0}{p} + k_1 \right) \right]} \frac{\sin \left[\pi \left(\frac{l_0}{p} + l_1 \right) \right]}{\sin \left[\frac{\pi}{N} \left(\frac{l_0}{p} + l_1 \right) \right]} \\
&\quad \times \exp \left\{ -j2\pi \left[\left(\frac{k_0}{p} + k_1 \right) \frac{M-1}{2} + \left(\frac{l_0}{p} + l_1 \right) \frac{N-1}{2} \right] \right\} \quad (3.35b)
\end{aligned}$$

Example 3.3

In this example we illustrate the interpolation scheme implied by Eq. (3.35b). Let the data matrix be expanded three times by padding zeros, that is, $P = 3$. The dft coefficients of the data (before padding) are given on a grid shown by large

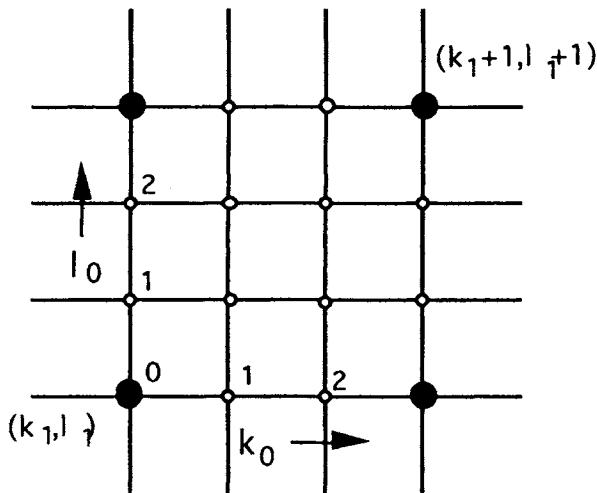


Figure 3.13. Interpolation scheme as per Eq. (3.35b). The dft coefficients of the data matrix are given by filled circles while interpolation is shown by empty circles. The data matrix has been expanded three times ($P = 3$) by padding zeros.

filled circles. By interpolation the dft coefficients are now computed on a finer grid with spacing of one-third of the original grid at the points shown by small empty circles.

3.4.5. Statistical properties of dft coefficients

When the observed potential field is modelled as a random field the dft coefficients also become random variables. They possess some important statistical properties, valid for large data size [4].

$$E\{F(k, l)F^*(k', l')\} \approx MN \sum \sum C_f(p, q) \exp\left\{-j\left[\left(\frac{2\pi}{M}\right)pk + \left(\frac{2\pi}{N}\right)ql\right]\right\} \delta_{kk'} \delta_{ll'} \quad (3.36a)$$

where $\delta_{kk'} = 0$ for $k \neq k'$ and $= 1$ for $k = k'$ and likewise $\delta_{ll'}$. The right-hand side of Eq. (3.36) is, by definition, the spectrum of random field. Hence, we have

$$S_f(k, l) \approx \frac{1}{MN} E\{|F(k, l)|^2\} \quad (3.36b)$$

Eq. (3.36b) is useful for practical computation of spectrum of a random field using the dft coefficients.

3.4.6. Estimation 2D spectrum

We now use the statistical properties of the dft coefficients of a homogeneous random process, in particular Eq. (3.36). The spectrum of a single random process (square data matrix, $N \times N$) may be estimated

$$S_f(k, l) = \frac{1}{N^2} E\{|F(k, l)|^2\}, \quad N \rightarrow \infty \quad (3.37)$$

Similarly where there are two stochastic processes, $f_1(m, n)$ and $f_2(m, n)$ the cross-spectrum is related to the dft coefficients of each process,

$$S_{f_1 f_2}(k, l) = \frac{1}{N^2} E\{F_1(k, l) F_2^*(k, l)\}, \quad N \rightarrow \infty \quad (3.38)$$

There are two possible approaches to implementation of the expected operation in Eqs. (3.37) and (3.38). In the first method the expected operation is replaced by neighbourhood averaging. Specifically, we form an estimate of the spectrum (or cross-spectrum) from

$$\hat{S}_f(k, l) = \frac{1}{p_0} \sum_m \sum_{n \in \Omega} |F(k + m, l + n)|^2 \quad (3.39)$$

where Ω represents some neighbourhood of a point k, l , say, a polygonal neighbourhood with p_0 number of discrete points (see Figure 3.14).

In selecting the neighbourhood it is essential to keep in mind the assumption that the spectrum is constant over the neighbourhood. Further, we assume that the digital map is sufficiently large so that the dft coefficients become uncorrelated. The map should be suitably windowed so that the power leakage through the sidelobes is minimized. This is important when large peaks are present in the spectrum. In many situations there is a slowly varying background whose effect is specially felt at the low frequency end of the spectrum in the form of a large magnitude peak. A considerable amount of power may leak into the neighbourhood of low frequency through the side lobes of the window function. Much of

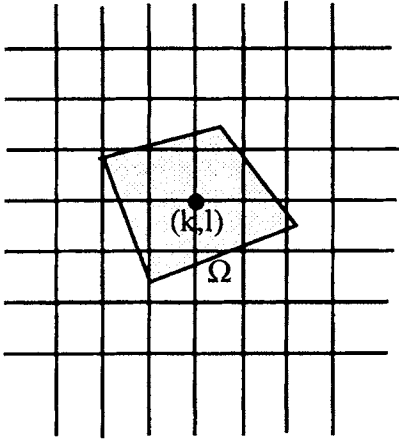


Figure 3.14. The neighbourhood of a point (k,l) over which the averaging, as indicated in Eq. (3.39), is carried out.

this can be avoided by removing the slowly varying component by means of low pass filtering or by subtracting a least squares polynomial.

In the second approach the digital map is divided into several submaps (these may be partially overlapping; see Figure 3.15). An estimate of the spectrum is now obtained as follows:

$$S_f(k, l) = \frac{1}{N^2} \sum_{p=1}^{p_0} |F_p(k, l)|^2 \quad (3.40)$$

where p_0 is the number of submaps into which the entire digital map is divided. We further assume that each submap is uncorrelated with all other submaps. If the size of a submap is such that it is greater than the correlation distance, it is likely that a submap is uncorrelated with all other submaps including those in the immediate neighbourhood.

Each submap is multiplied by a window function basically for the same reason as in the first method. One consequence of windowing is to reduce the weightage of otherwise perfectly good data which happens to lie along the edges of the submap. Thus windowing in fact throws away a portion of the good data. This drawback is partially overcome by overlapping the adjacent submaps to the extent of 50%. To improve the low frequency estimate the mean is subtracted from each submap.

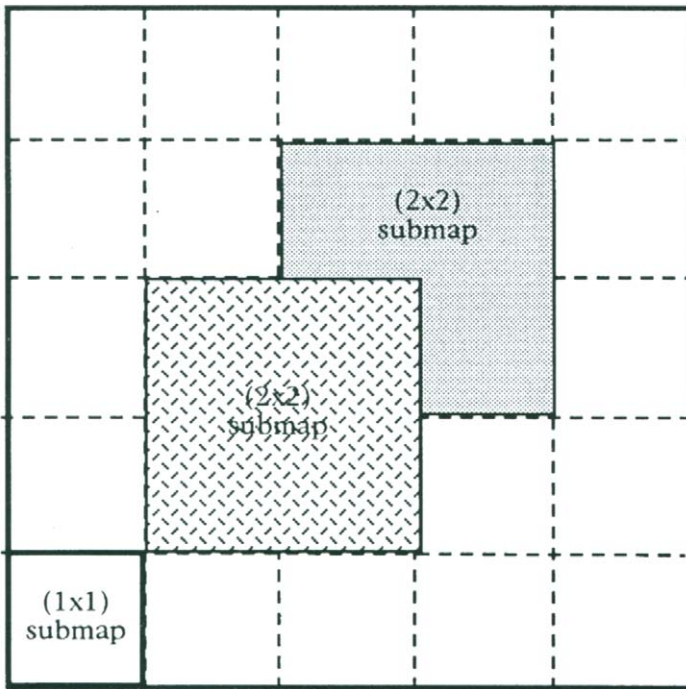


Figure 3.15. Overlapping of submaps for spectrum estimation. A large aeromagnetic map is first divided into many basic units (1×1 submaps). For spectrum estimation four or more unit submaps are combined into a larger submap with reuse. In this figure, two 2×2 submaps are formed with 50% overlap.

The above discussion pertaining to the spectrum is equally valid for the cross-spectrum between two digital maps. When the maps refer to two physically different phenomena it is possible that the scale factor of one may be quite different from that of the second. In such a case it is recommended that the two maps are suitably scaled so that the mean power in each is roughly the same. The discrete spectrum is estimated at frequency numbers, $(k, l = 0, 1, \dots, N/\sqrt{(P_0)})$. We assume that we have a square map of $N/\sqrt{(P_0)} \times N/\sqrt{(P_0)}$. The frequency numbers are easily converted into frequencies (cycles per unit sample interval) by multiplying with a factor equal to $\sqrt{(P_0)}/N$. Note that the frequency numbers from 0 to $N/2\sqrt{P_0}$ refer to positive frequencies (0 to $1/\Delta x$) and frequency number from $(N/2\sqrt{P_0} + 1$ to $(N/\sqrt{P_0} - 1$ refer to negative frequencies (0 to $-1/\Delta x$). From the estimated spectrum (or cross-spectrum) if you want to compute the autocorrelation function

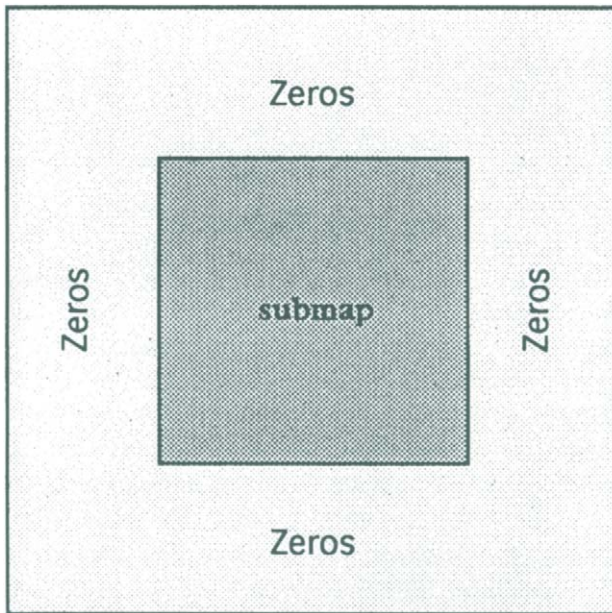


Figure 3.16. Zero padding around each submap is required to avoid the aliasing effect in the autocorrelation function computed using the dft algorithm.

(or cross correlation function) by inverse Fourier transform we get the cyclic autocorrelation function which is different from the normal autocorrelation function. It carries an aliasing error on account of periodic repetitions of the autocorrelation function just as in the Fourier transform of a sampled signal. To overcome this, each submap is bordered by a blank or null map of width equal to half the width of the submap (see Figure 3.16).

3.4.7. Bias and variance

In practice, the spectrum of a potential field is computed from the available finite map. Consequently, the size of a submap as well as the number of such submaps will be limited. The resulting estimate will suffer from two drawbacks, namely, the estimate becomes biased and its statistical variability increases. The bias arises on account of finite size of submaps. Recall that it was recommended that each submap should be multiplied by a window function. We now show the basis for such a recommendation. Using Eq. (3.31) in Eq. (3.40) and taking the expected value, we get

$$\begin{aligned}
S_f(k, l) &= E\{\hat{S}_f(k, l)\} \\
&= \frac{1}{4\pi^2} \int \int_{-\pi}^{+\pi} S_f(u, v) |W(k - u, l - v)|^2 du dv
\end{aligned} \tag{3.41}$$

From Eq. (3.41) it is clear that the average of the estimated spectrum is not equal to the true spectrum, $S_x(u, v)$, except when $W(u, v)$ is a delta function. For finite sized submaps $W(u, v)$ will never be a delta function. In general, for any chosen window function we have a main central lobe surrounded by many side lobes. Let us form a simplified mental image of the convolution operation performed in Eq. (3.41). The spectral estimate at frequency numbers (k, l) consists of two parts, namely, a contribution from the central lobe and a contribution from the side lobes. The first part may be approximated as an average of the true spectrum over a frequency cell of size $2\pi/N \times 2\pi/N$. The second part consists of all the power that has leaked through the various side lobes. The second part can cause serious problems, particularly when there is a small spectral peak in the neighbourhood of a large peak. It would be difficult to resolve the two peaks and to estimate the power in the smaller peak. The loss of resolution could also be due to the averaging effect of the central lobe. Thus, the bias in the spectrum estimate is closely related to the window function. Naturally, by suitable choice of the window function the bias can be minimized but can never be eliminated. The uniform window (or equal weighting window) is the worst type of window in so far as its sidelobe structure is concerned; it has, however, the narrowest possible main lobe. The art of selecting an optimum window is beyond the scope of the present work (see Ref. [4] for some details on the optimum window). The bias characteristics of the cross-spectrum estimate are quite similar to those of spectrum estimate.

We now consider the variance calculation of the spectral estimate. Without proof we give the following results taken from [14].

$$\begin{aligned}
\text{var } \hat{S}_f(k, l) &= E\{(\hat{S}_f(k, l) - E\{\hat{S}_f(k, l)\})^2\} \\
&= \frac{1}{p_0} S_f^2(k, l) \quad \text{when } k, l \neq 0 \text{ or } \frac{N}{2\sqrt{p_0}} + 1 \\
&= \frac{2}{p_0} S_f^2(k, l) \quad \text{otherwise}
\end{aligned} \tag{3.42}$$

and for the cross-spectrum

$$\begin{aligned}
\text{var } \hat{S}_{f_1 f_2}(k, l) &= E\{|\hat{S}_{f_1 f_2}(k, l)|^2\} - E\{\hat{S}_{f_1 f_2}(k, l)\}^2 \\
&= \frac{1}{p_0} S_{f_1}(k, l) S_{f_2}(k, l) \quad \text{when } k, l \neq 0 \text{ or } \frac{N}{2\sqrt{p_0}} + 1 \\
&= \frac{1}{p_0} [S_{f_1 f_2}(k, l) + S_{f_1}(k, l) S_{f_2}(k, l)] \quad \text{otherwise}
\end{aligned} \tag{3.43}$$

From Eqs. (3.42) and (3.43) we note that the variance of the spectral estimate can be reduced by increasing the number of submaps.

3.4.8. Estimation of coherence

The coherence function is estimated by

$$\text{coh}_{f_1 f_2}(k, l) = \frac{\hat{S}_{f_1 f_2}(k, l)}{\sqrt{\hat{S}_{f_1}(k, l) \hat{S}_{f_2}(k, l)}} \tag{3.44}$$

The statistical properties of the coherence estimate are highly involved. We note some of the simplified and approximate results due to Hinich and Clay [15] valid for large p_0 and high coherence.

$$\text{var } |\text{coh}_{f_1 f_2}| \approx \frac{1}{2p_0} (1 - |\text{coh}_{f_1 f_2}|^2)^2$$

$$\text{var } \hat{\phi} \approx \frac{-1}{2p_0} (1 - |\text{coh}_{f_1 f_2}|^{-2})$$

where $\hat{\phi}$ is the phase of the complex coherence estimate

$$\hat{\phi} = \tan^{-1} \left[\frac{\text{Im } \text{coh}_{f_1 f_2}}{\text{Re } \text{coh}_{f_1 f_2}} \right]$$

Note that when the actual coherence magnitude is large the variance tends to be quite small even when the number of submaps is small. In practical problems, where the amount of available data is small, we can at most say whether the

coherence is high (significant) or low (insignificant), but can rarely measure moderate coherence. Let $p_0 = 10$ and the true coherence magnitude be 0.9; then the computed coherence lies between 0.88 and 0.95 with 90% confidence. When the true coherence magnitude is 0.4 the computed coherence magnitude lies between 0.16 and 0.7 with 90% confidence. Thus the variability is less at higher coherence values, which makes it easy to ascertain the occurrence of higher coherence. It is important to remember that for $p_0 = 1$ the coherence estimate is always 1.0 whether the time series are correlated or not. Further details on the variability of coherence may be found in Ref. [4].

3.4.9. Spectral windows

In Section 3.2 the spectrum of a random function was defined in terms of its autocorrelation function or its generalized Fourier transform. Both definitions assume that the random function is available over an infinite plane. In practice, however, the potential field data are available over a finite area, either because no measurements were made outside the area of investigation or the data are found to be homogeneous only over a finite area. Such a situation may be modelled as a product of a homogeneous random process and a function, known as a window, which has a finite value (≤ 1.0) in the region where the data are given and zero where there are no data. The homogeneous random process used in the model coincides with the observed data and with its homogeneous extrapolation outside. However, since it is multiplied by zero, it is not necessary to carry out the actual extrapolation. We model the finite data as follows:

$$f_0(m, n) = f(m, n)w_0(m, n) \quad (3.45)$$

where $f_0(m, n)$ equal to the observed field over a finite area and $w_0(m, n)$ be a discrete window function

$$w_0(m, n) \leq 1.0, \quad 0 \leq m \leq M - 1, \quad 0 \leq n \leq N - 1$$

$$w_0(m, n) = 0.0 \quad \text{otherwise}$$

where we have assumed for simplicity that the area of investigation is a rectangle of size $M \times N$. We use the spectral representation of a random potential field $f(m, n)$ (see Section 2) and the Fourier representation of the window function in Eq. (3.45)

$$\begin{aligned}
 f(m, n) &= \frac{1}{4\pi^2} \int \int_{-\pi}^{+\pi} dF(u, v) \exp[+j(um + vn)] \\
 w_0(m, n) &= \frac{1}{4\pi^2} \int \int_{-\pi}^{+\pi} W_0(u, v) \exp[+j(um + vn)] du dv \\
 f_0(m, n) &= f(m, n) w_0(m, n) \\
 &= \frac{1}{4\pi^2} \int \int_{-\pi}^{+\pi} F_0(u, v) \exp[+j(um + vn)] du dv
 \end{aligned}$$

where

$$F_0(u, v) = \frac{1}{4\pi^2} \int \int_{-\pi}^{+\pi} dF(u', v') W_0(u - u', v - v')$$

The dft coefficients of $f_0(m, n)$, $0 \leq m \leq M - 1$ and $0 \leq n \leq N - 1$ are given by

$$F_0(k, l) = \frac{1}{4\pi^2} \int \int_{-\pi}^{+\pi} dF(u', v') W_0\left(\frac{2\pi k}{M} - u', \frac{2\pi l}{N} - v'\right) \quad (3.46)$$

$$0 \leq k \leq M - 1 \text{ and } 0 \leq l \leq N - 1$$

Using the properties of the dft coefficients (see Section 3.4.5) we obtain an expression for the spectrum of a finite random potential field

$$\begin{aligned}
 S_{f_0}(k, l) &= E \left\{ \frac{1}{MN} |F_0(k, l)|^2 \right\} \\
 &= \frac{1}{4\pi^2} \int \int_{-\pi}^{+\pi} S_f(u', v') \left| W_0\left(\frac{2\pi k}{M} - u', \frac{2\pi l}{N} - v'\right) \right|^2 du' dv' \quad (3.47)
 \end{aligned}$$

Eq. (3.47) gives us a relationship between the spectrum determined from finite 2D data which is observed and the spectrum of infinite 2D data which is not observed. $|W_0(u, v)|^2$ is the spectrum of the window function. Apart from the smoothing effect produced by the convolution operation and leakage of power, which is well documented [4], the angular variation of the spectrum of the potential field may be disturbed unless the window is isotropic.

An ideal window for spectral analysis of a potential field must possess the following characteristics. (a) The spectrum of the window must be as close to a delta function as possible. Then, from Eq. (3.47) we note that

$$S_{f_0}(k, l) = S_f\left(\frac{2\pi k}{M}, \frac{2\pi l}{N}\right)$$

(b) The leakage of power is minimum, which is possible by controlling the height of sidelobes. (c) The spectrum of the window must be isotropic or close to being isotropic.

In 1D spectrum analysis there is considerable interest in the design of spectral windows satisfying (a) and (b); for example, the optimum windows defined in terms of the discrete spheroidal wave sequences (see Ref. [8] for discussion on this topic). A window for 2D spectrum analysis may be created using a 1D window simply by spinning it around the centre point, but such a window will be on a polar raster instead of being on a rectangular grid.

3.5. Depth estimation from radial spectrum

The depth to a source (magnetic layer) is a piece of information of great value in geological/geophysical interpretation of subsurface structure. Much of the literature on potential field interpretation is directed at estimation of the depth of a source, often modelled as a well defined geometrical object. We pursue this line of study in Chapter 6 as a problem in parameter estimation within the framework of digital signal processing. The parameter estimation approach soon becomes unmanageable when we are faced with more than two or more closely spaced sources. In practice such a situation is not uncommon; for example, a layer of magnetized rocks (basic rocks) where the magnetization is rapidly varying. Radial spectrum offers a unique possibility to estimate the depth to the magnetic layer. There are two types of models, namely, a randomly polarized magnetic layer and a random interface separating two homogeneous media for which depth estimation using the radial spectrum is feasible.

3.5.1. Single layer model

First we consider a magnetized layer of finite thickness which is uniformly magnetized. However, the susceptibility variation is purely random. The spectrum of the total component may be derived from Eq. (2.83) and is given by [16,17]

$$S_T(u, v, h) = |(juI_x + jvI_y - sI_z)(ju\alpha + jv\beta - s\gamma)|^2 \frac{\exp(-2sh)}{s^2} \times \int_{-\infty}^{\infty} \frac{|(1 - \exp[-(s - jw)\Delta h])|^2}{s^2 + w^2} S_{\Delta\kappa}(u, v, w) dw \quad (3.48a)$$

where $S_{\Delta\kappa}(u, v, w)$ is the spectrum of the susceptibility variation in the rock layer. For a thin layer, Eq. (3.48a) reduces to

$$S_T(u, v, h) = |(juI_x + jvI_y - sI_z)(ju\alpha + jv\beta - s\gamma)|^2 \frac{\exp(-2sh)}{s^2} \times \Delta h^2 \int_{-\infty}^{+\infty} S_{\Delta\kappa}(u, v, w) dw \quad (3.48b)$$

and for semi-infinite half space it reduces to

$$S_T(u, v, h) = |(juI_x + jvI_y - sI_z)(ju\alpha + jv\beta - s\gamma)|^2 \frac{\exp(-2sh)}{s^2} \times \int_{-\infty}^{+\infty} \frac{S_{\Delta\kappa}(u, v, w)}{s^2 + w^2} dw \quad (3.48c)$$

In Eq. (3.48a) if we assume that $S_{\Delta\kappa}(u, v, w) = S_{\Delta\kappa}(u, v)$, that is, the susceptibility variation in the vertical direction is uncorrelated or white and noting that the resulting integral may be evaluated as

$$\int_{-\infty}^{+\infty} \frac{|1 - \exp[-(s - jw)\Delta h]|^2}{s^2 + w^2} dw = \frac{\pi}{s} [1 - \exp(-2s\Delta h)]$$

$$S_T(u, v, h) = \frac{\pi}{s^3} |(juI_x + jvI_y - sI_z)(ju\alpha + jv\beta - s\gamma)|^2 \times [\exp(-2sh) - \exp(-2s(h + \Delta h))] S_{\Delta\kappa}(u, v) \quad (3.48d)$$

This corresponds to the sandwich model proposed by Jacobsen [24] which is sketched in Figure 3.17.

Note that in Eq. (3.48) the dominant factor is $\exp(-2sh)$ which decays expo-

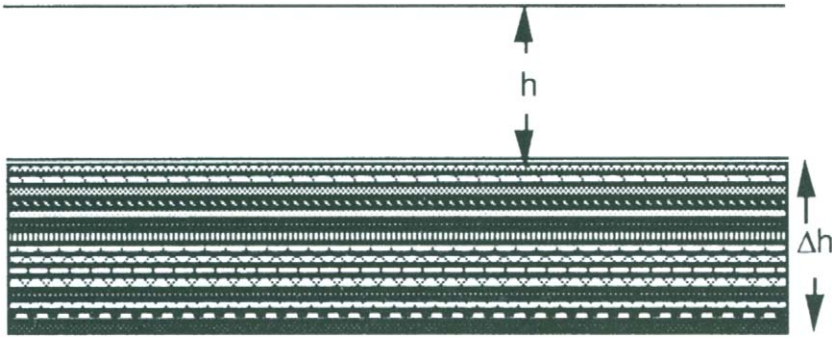


Figure 3.17. A schematic representation of the Sandwich model [24]. The susceptibility in each layer is a stochastic function and is uncorrelated with all other layers

nentially. The rate of decay is proportional to the depth to the magnetized layer. From Eq. (3.48b) we can easily determine the radial spectrum

$$R_{\text{pole}}(s) = I_z^2 s^2 \exp(-2sh) R_{\Delta\kappa}(s) \quad (3.48e)$$

where

$$R_{\Delta\kappa}(s) = \frac{\Delta h^2}{2\pi} \int_0^{2\pi} \int_{-\infty}^{\infty} S_{\Delta\kappa}(s \cos(\theta), s \sin(\theta), w) dw d\theta$$

is the radial spectrum of the susceptibility variations. For simplicity we have assumed only vertical polarization or the field has been reduced to pole.

3.5.2. Fractal models of susceptibility variations

Consider two different extreme cases which lead to relatively simple results. In the first case, we consider a thin layer whose spectrum of the susceptibility variations is a function of s only, that is,

$$S_{\Delta\kappa}(u, v) = \frac{\sigma_{\Delta\kappa}^2}{s^2} \exp(-2ls)$$

where l is a positive constant depending on the rock type and $\sigma_{\Delta\kappa}^2$ is the variance

of susceptibility variations. The $1/s^2$ term is introduced to account for the observed fractal nature of the magnetization [18,19]. Using the above model of magnetization in Eq. (3.48b), we obtain

$$R_{\text{pole}}(s) = \sigma_{\Delta\kappa}^2 I_z^2 \exp(-2s(h+l)) \quad (3.49a)$$

Interestingly the radial spectrum is a pure exponentially decreasing function. Next, we consider a semi-infinite medium where the 3D susceptibility variation has a spectrum of the form

$$S_{\Delta\kappa}(u, v, w) = \frac{\Omega}{s^2} \exp(-2ls), \quad |w| \leq \beta$$

$$= 0 \quad \text{otherwise}$$

where β and $l \geq 0$ are unknown constants, depending upon the rock type. Using the above 3D stochastic model in Eq. (3.48c), we obtain

$$R_{\text{pole}}(s) = \Omega I_z^2 \frac{\exp(-2s(l+h))}{s} \tan^{-1}\left(\frac{\beta}{s}\right) \quad (3.49b)$$

For $l\beta \gg 1$ and finite sl we approximate $\tan^{-1}(\beta/s) \approx \pi/2$. Then, Eqs. (3.49a) and (3.49b) become identical. The assumption that $l\beta \gg 1$ implies that the medium is more random in the vertical direction than in the horizontal direction. The radial spectrum now has $1/s$ dependance.

There is some evidence suggesting that the natural magnetization possesses a fractal character, hence its spectrum may be expressed in the form

$$S_{\Delta\kappa}(u, v, w) = \frac{\Omega}{(s^2 + w^2)^{\nu/2}}$$

where $\nu \approx 3$ [19] and Ω is a constant. Using the above model of magnetization, Eq. (3.48a) can be evaluated as follows:

$$S_T(u, v, h) = |(juI_x + jvI_y - sI_z)(ju\alpha + jv\beta - s\gamma)|^2 \frac{\exp(-2sh)}{s^2}$$

$$\begin{aligned}
& \times \frac{1}{s^{\nu+1}} \int_{-\infty}^{\infty} \frac{\Omega}{\left(1 + \frac{w^2}{s^2}\right)^{(\nu/2)+1}} d\left(\frac{w}{s}\right) \\
& = \left| (juI_x + jvI_y - sI_z)(ju\alpha + jv\beta - s\gamma) \right|^2 \frac{\exp(-2sh)}{s^4} \\
& \times \frac{1}{s^{\nu-1}} \int_{-\infty}^{\infty} \frac{\Omega}{(1+x^2)^{\frac{\nu}{2}+1}} dx \\
& = \frac{\Omega \sqrt{\pi} \Gamma\left(\frac{\nu+1}{2}\right)}{\Gamma\left(\frac{\nu}{2}+1\right)} \left| (juI_x + jvI_y - sI_z)(ju\alpha + jv\beta - s\gamma) \right|^2 \frac{\exp(-2sh)}{s^{\nu+3}}.
\end{aligned} \tag{3.49c}$$

Notice the presence of $1/s^{\nu-1}$ which becomes dominant in the neighbourhood of $s \approx 0$. In support of the above model we give an example of the radial spectrum

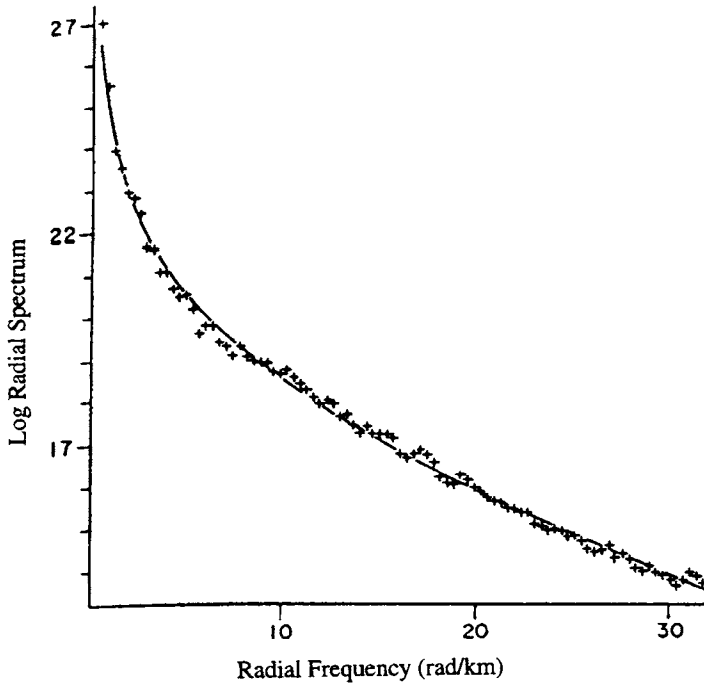


Figure 3.18. Radial spectrum of the aeromagnetic field from the area where the German deep drilling project is located. Estimated value of the exponent, $\gamma = \nu - 1 = 2.07$.

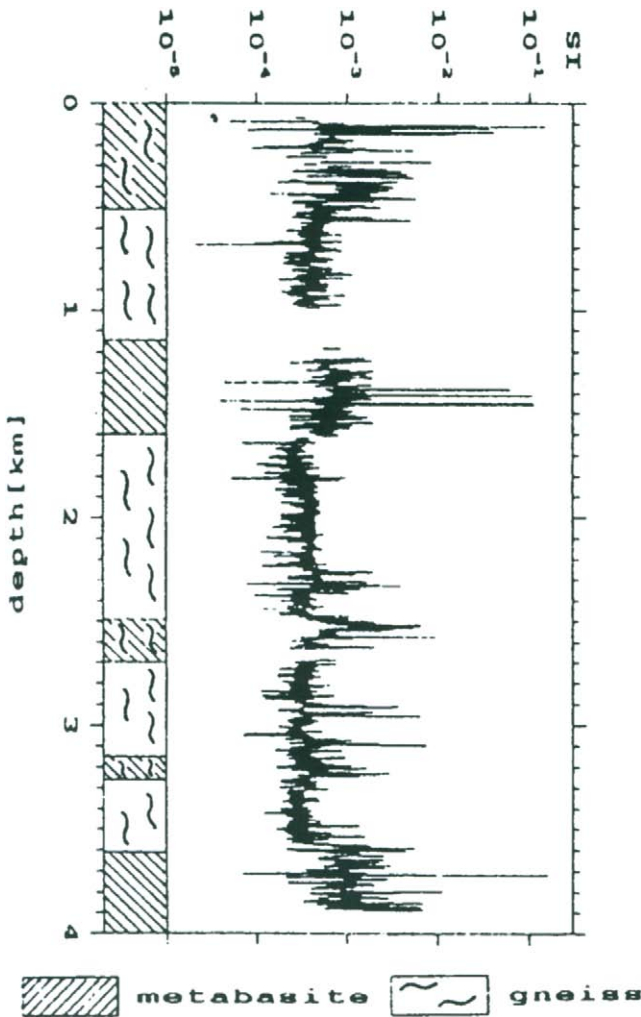


Figure 3.19. Vertical profile of rock susceptibilities obtained from drill cores of the German deep drilling project [19]. Missing values are due to incomplete recovery of the drill cores.

of an aeromagnetic field from the area where the German deep drilling project is located [19].

Analysis of the rock susceptibilitiues obtained from the drilling core (see Figure 3.19), however, does not wholly agree with the spectrum model used in deriving Eq. (3.49c); but is perhaps closer to the band limited white noise model used in deriving Eq. (3.49b).

For a gravity field the radial spectrum is essentially the same as that for the pole reduced magnetic field with the only difference that the s^2 term in Eq. (3.48e) is absent. Hence the radial spectrum of the gravity field becomes purely exponentially decreasing when the density variation in all three direction is totally uncorrelated, that is, white noise. However, if we assume a fractal model for density variation,

$$S_{\Delta\rho}(u, v, w) = \frac{\Omega}{(s^2 + w^2)^{\nu/2}}$$

the radial spectrum of the gravity field will be given by

$$\begin{aligned} R_z(s) &= \frac{\exp(-2sh)}{s^{\nu+2}} \int_{-\infty}^{\infty} \frac{\Omega}{\left(1 + \frac{w^2}{s^2}\right)^{(\nu/2)+1}} d\left(\frac{w}{s}\right) \\ &= \Omega \frac{\sqrt{\pi} \Gamma\left(\frac{\nu+1}{2}\right) \exp(-2sh)}{\Gamma\left(\frac{\nu}{2} + 1\right) s^{\nu+2}} \end{aligned} \quad (3.50)$$

As of now there is no practical evidence to suggest that $\nu > 0$.

3.5.3. Many layers

Analysis of a single sheet of magnetization can be extended to a more complex model consisting of two or more layers or interfaces (Figure 3.20).

Assuming the susceptibility variations in different layers are independent we write down the expression for total radial spectrum as follows:

$$R_{\text{pole}}(s) = \sum_{i=1}^p \sigma_i^2 I_z^2 \exp(-2s(h_i + l_i)) \quad (3.51)$$

The radial spectrum in Eq. (3.51) is a sum of p real exponential functions. A plot of the radial spectrum on a semi-logarithmic graph sheet shows some interesting features, namely, for small p there exist spectral windows in which linear segments of the radial spectrum can be seen and from the slope of the segments we can estimate the depth to different layers. For this to be possible, the magnetic layers must be well separated with significantly differing intensity of magnetization, that is, σ_i^2 in Eq. (3.51). Figure 3.21 shows two examples of two and three layers whose radial spectra seem to exhibit linear segments with a slope close to the assumed depths. The intensity of magnetization of the deeper layer is assumed to be ten times stronger than that of the layer above it.

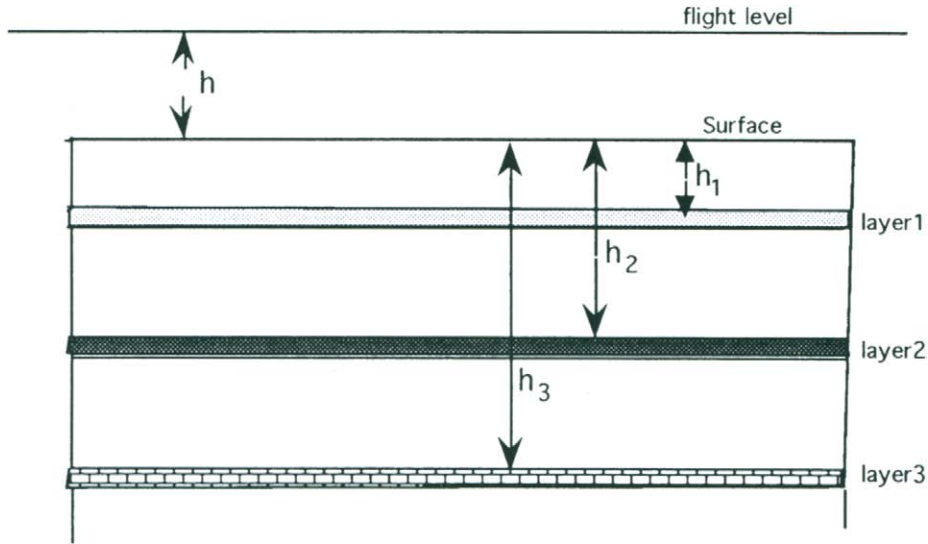


Figure 3.20. A model of three thin horizontal magnetic layers. The magnetization in each layer is independent and its spectrum follows from Eq. (3.48b).

3.5.4. Depth variation of susceptibility/density:

When the number of layers is too large both the above graphical method and fitting an autoregressive model become impractical. We give an analytic method based on an inverse Laplace transform to estimate the variance of the susceptibility/density as a function of depth. Consider a stack of horizontal layers of equal thickness $\Delta h \ll \lambda_{\text{mir}}$, that is, much smaller than the smallest wavelength of the susceptibility variations (see Figure 3.17).

Further, we assume that the spectrum of the susceptibility variation in the i th layer is given by

$$\frac{(\delta h)^2}{2\pi} \int_{-\infty}^{\infty} S_{\Delta\kappa}(u, v, w) dw = \frac{\sigma_{\Delta\kappa}^2(i\delta h)}{s^2} \exp(-2ls)\delta h \quad (3.52)$$

where $\sigma_{\Delta\kappa}^2(i\delta h)$ is the variance of susceptibility in the i th layer. The susceptibility in the i th layer is uncorrelated with the susceptibility variation in any other layer. Using Eq. (3.52) in Eq. (3.48b) we obtain an expression for a thick stack of vertically polarized layers as shown in Figure 3.22.

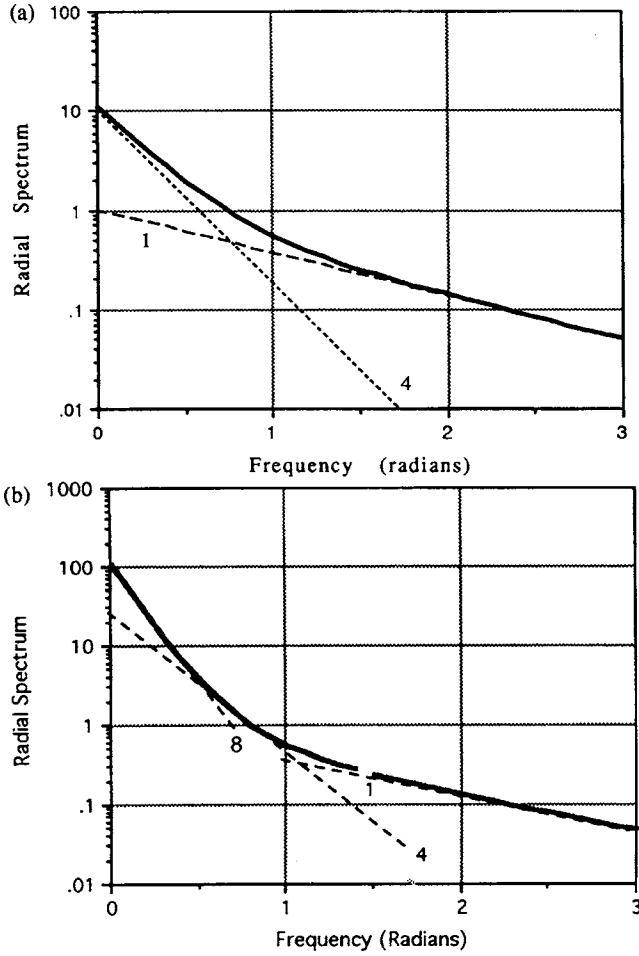


Figure 3.21. Radial spectrum due to (a) two thin layers and (b) three thin layers. The dashed lines represent the radial spectrum due to individual layers at depths as indicated.

$$S_{f_{\text{pole}}}(s, h) = 2\pi I_0^2 \exp(-2s(h+l)) \sum_{i=0}^{\infty} \sigma_{\Delta\kappa}^2(i\delta h) \exp(-2s\delta h i) \delta h \quad (3.53a)$$

or

$$\sum_{i=0}^{\infty} \sigma_{\Delta\kappa}^2(i\delta h) \exp(-2s\delta h i) \delta h = \frac{S_{f_{\text{pole}}}(s, h)}{2\pi I_0^2 \exp(-2s(h+l))} \quad (3.53b)$$

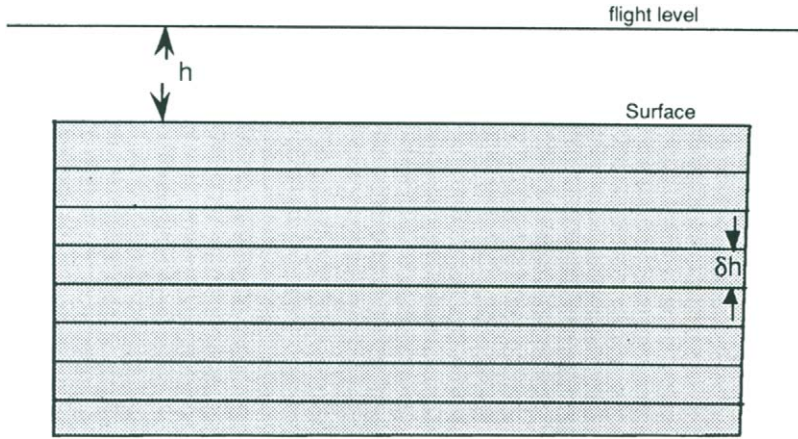


Figure 3.22. A thick rock strata is modelled as a stack of many thin layers. In each layer the magnetization is a function of two horizontal coordinates but the variance is a function of depth. In all other respects the strata are homogeneous.

The right-hand side is completely known. The left-hand side may be treated as a discrete Laplace transform of $\sigma_{\Delta\kappa}^2(z)$ and s as a complex frequency. By computing the inverse Laplace transform of the right-hand side, that is, evaluating the following integral on the imaginary axis

$$\sigma_{\Delta\kappa}^2(z) = \frac{1}{2\pi^2} \int_{-\pi}^{\pi} \frac{S_{f_{\text{pole}}}(j\omega, h)}{I_0^2 \exp(-2j\omega(h + l))} \exp(j\omega z) d\omega \quad (3.54)$$

Note that

$$S_{f_{\text{pole}}}(j\omega, h) = \frac{S_{f_{\text{pole}}}(s, h)}{2}$$

as the power at radial frequency s is equally distributed between $+j\omega$ and $-j\omega$. In practical applications, conversion of a real variable, s , into a complex variable $j\omega$ is achieved by expressing the radial spectrum as a sum of exponential functions. This approach was first suggested by Klushin in 1959 [20] who must be given credit for the use of the radial spectrum of a potential field for depth estimation. We illustrate the inversion procedure through an example (Example 3.4).

Example 3.4

Consider the sandwich model of a thick magnetic layer consisting of a large number of thin uncorrelated layers (Figure 3.17) but with lateral variation of susceptibility as in Eq. (3.52). The spectrum of the total magnetic field was derived earlier Eq. (3.48d) where we now assume in accordance with the model in Eq. (3.52) that

$$S_{\Delta\kappa}(u, v) = \frac{\sigma_{\Delta\kappa}^2}{s^2}$$

For simplicity we consider only the field reduced to pole. The spectrum of the field is given by

$$S_{f_{\text{pole}}}(s, h) = \frac{\pi}{s} |I_0|^2 [\exp(-2sh) - \exp(-2s(h + \Delta h))] \sigma_{\Delta\kappa}^2$$

On substituting in Eq. (3.54) we obtain

$$\hat{\sigma}_{\Delta\kappa}^2(z) = \frac{\sigma_{\Delta\kappa}^2}{2\pi} \int_{-\pi}^{\pi} \frac{1}{j\omega} [1 - \exp(-2j\omega\Delta h)] \exp(j\omega z) d\omega$$

where $\hat{\sigma}_{\Delta\kappa}^2(z)$ is an estimate of $\sigma_{\Delta\kappa}^2$. The integral is easily shown to be the difference of two step functions, $\Omega(z) - \Omega(z - 2\Delta h)$ where $\Omega(z)$ is a step function. Hence

$$\hat{\sigma}_{\Delta\kappa}^2(z) = \sigma_{\Delta\kappa}^2 [\Omega(z) - \Omega(z - 2\Delta h)]$$

3.5.5. Interface model

An interface separating two homogeneous media will give rise to potential field anomaly. In Chapter 2 we derived the gravity and magnetic field produced by an interface, modelled as a homogeneous random surface, separating two homogeneous media, for example, a column of sedimentary rocks overlying an ancient basement consisting of heavier granitic rocks. Let us consider the above model for the purpose of showing the possibility of estimating the depth to the basement. The spectrum of the gravity field observed on the surface, that is, on

the top of the sedimentary column may be obtained from Eq. (2.68c) when the basement is deep compared to the undulations. We give the final expression

$$S_{f_z}(u, v) = \Delta \rho^2 G^2 S_{\Delta z}(u, v) \exp(-2hs)$$

The radial spectrum is given by

$$R_{f_z}(s) = \Delta \rho^2 G^2 R_{\Delta z}(s) \exp(-2hs) \quad (3.55a)$$

Assuming that

$$S_{\Delta z}(u, v) = \sigma_{\Delta z}^2 \exp(-2ls), \quad l \geq 0$$

the radial spectrum (Eq. 3.55a) reduces to

$$R_{f_z}(s) = \Delta \rho^2 G^2 \sigma_{\Delta z}^2 \exp(-2s(h + l)) \quad (3.55b)$$

It must be noted that the depth estimates given by Eq. (3.50) or Eq. (3.55b) will be an overestimate of the true depth depending upon the unknown constant l . A convenient method of estimating the depth to the layer or interface is to plot the radial spectrum on semi-logarithmic paper with the amplitude on the log axis and the frequency on the linear axis.

3.5.6. Physical significance of 'spectral' depths

In a physical model where there are distinct thin layers with 'white' magnetization, the spectral depths are actually the physical depths. When the magnetization is non-white, the spectral depth is always greater than the physical depth. When the layer is thick, it is difficult estimate the bottom of the layer. To show this let us go back to Eq. (3.48d) which we shall express in a slightly different form,

$$\frac{s^3}{\pi \Gamma_0^2(u, v)} S_T(u, v, h) = \exp(-2sh) S_{\Delta \kappa}(u, v) - \exp(-2s(h + \Delta h)) S_{\Delta \kappa}(u, v) \quad (3.56)$$

where $\Gamma_0(u, v) = (jul_x + jvl_y - sI_z)(ju\alpha + jv\beta - s\gamma)$. For simplicity we assume that $S_{\Delta\kappa}(u, v) = \text{constant}$. Eq. (3.56) may be treated as a difference between two exponential functions having different exponents. Such a spectrum, when plotted on semi-log paper, will not show two linear segments. For example, let $h = \Delta h = 1$; the spectral plot for this is shown in Figure 3.22a.

In the low frequency region where we normally look for the deeper layer there is a deep null; however, the linear segment in the high frequency region is due to top of the layer. The depth to the bottom may be estimated by least squares fitting. We have fitted a difference of two exponential functions, $\exp(-a_1s) - \exp(-a_2s)$, to the radial spectrum in the range 0–1.0 radial frequency. The estimated values of a_1 and a_2 for different background noise level are shown in Table 3.1.

It, thus, appears that the spectral depth which is estimated from the slope of the linear segment or by least squares fitting, refers to a surface of sharp change in the susceptibility or the variance of the susceptibility.

3.5.7. Estimation of radial spectrum

In Section 3.2 we introduced the radial spectrum as a radially averaged 2D spectrum of the potential field. It is more practical to estimate the radial spectrum

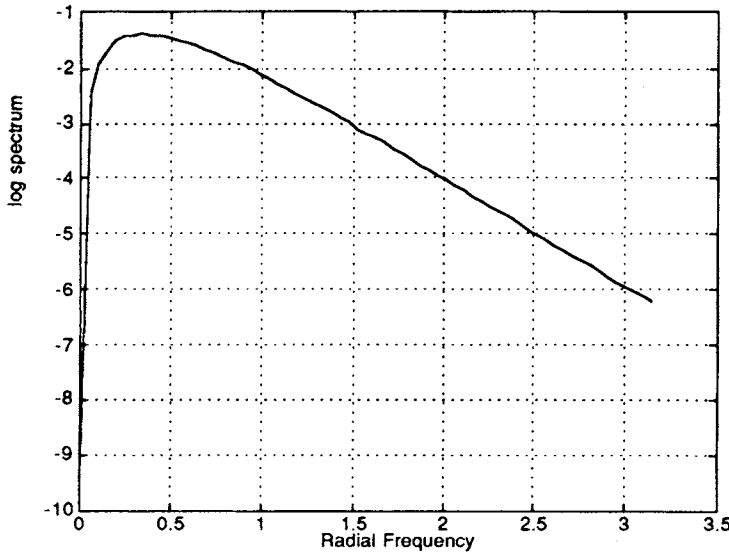


Fig. 3.22. (a) A plot of the right-hand side of Eq. (3.56). A layer of unit thickness at a depth of one unit and 'white' susceptibility variations ($S_{\Delta\kappa}(u, v) = 1$) are assumed.

TABLE 3.1

Least squares estimates of depth to the top and bottom of a magnetic layer

Actual values	Estimated noise std = 1	Estimated noise std = 2
$a_1 = 2.0$	1.998	2.004
$a_2 = 4.0$	3.960	4.005

The background noise is of zero mean and standard deviation equal to one and two.

directly from the Fourier transform of the potential field data. Let $f(m,n)$, $0 \leq m, n \leq N-1$, be a square data matrix and $F(k,l)$, $0 \leq k, l \leq N-1$ be its Fourier transform. The radial spectrum is estimated by averaging the magnitude square of $F(k,l)$ over a set of concentric rings with increasing radius (see Figure 3.23)

$$R(i) = \frac{1}{N_i} \sum_{k,l \in \text{ith ring}} |F(k,l)|^2, \quad i = 1, 2, \dots, \frac{N}{2} - 1$$

where N_i stands for the number of points in the i th ring. Note that we have

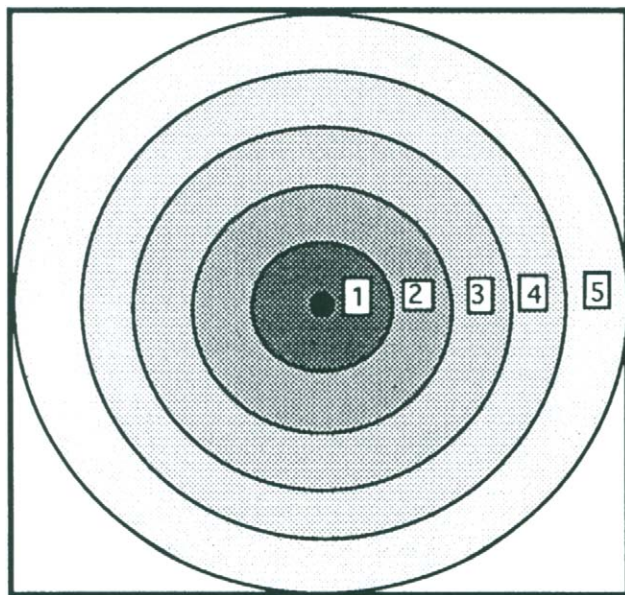


Figure 3.23. The magnitude square of 2D dft coefficients are averaged over a series of rings with incremental radius. Note that the central (zero frequency) dft coefficient is blocked as it may contain uncorrected power from the regional component.

excluded the 0th dft coefficient as it may contain power from uncorrected or partially corrected regional components.

3.5.8. Effect of quantization

We have shown earlier that the effect of quantization is to introduce white noise to the signal. The white noise will appear as a fixed component in the radial spectrum. To show this we have conducted a numerical experiment where the magnetic field due to a thin magnetic layer (unit thickness) at a depth of eight units was quantized by a step size of 10γ . The sheet is made of unit cubes (22 500 prisms) with random susceptibility but polarized uniformly (inclination 15° and declination 37°). The magnetic field is in the range -86 to -1γ .

Because of the quantization error power, much of the high frequency radial spectrum is submerged under quantization noise (see Figure 3.24). Thus, the frequency window available for the depth estimation is drastically reduced.

3.6. Angular spectrum

A two-dimensional spectrum may be expressed in a condensed form as two one-dimensional spectra, viz. the radial spectrum and the angular spectrum, defined in Eqs. (3.10) and (3.11), respectively. In order to free the angular

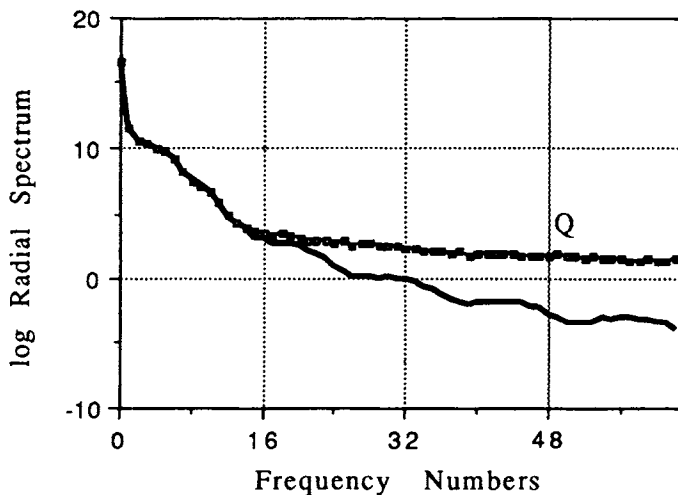


Figure 3.24. The radial spectrum of an infinite precision magnetic field due to a horizontal sheet (thick line) and quantized magnetic (step size 10γ), marked as Q.

spectrum of any radial variation, a normalization with respect to the radial spectrum may be applied. Thus, the angular spectrum is expected to bring out the angular variations, if any, of the 2D spectrum of the potential fields. The magnetic polarization vector imposes a strong directional variation of 2D spectrum. Thus, a study of angular spectrum of total magnetic field (i.e. aeromagnetic field) is very useful.

3.6.1. Angular spectrum of uniformly magnetized layer

Consider a horizontal infinite layer where the magnetic susceptibility is an arbitrary function (random function) of x and y coordinates but the direction of polarization is the same everywhere, that is, uniformly magnetized. The spectrum of the magnetic field (total field) caused by a layer of random magnetization may be obtained following the approach shown in [15,16]. We give the final result,

$$S_{f_T}(u, v) = |\Gamma(u, v)|^2 S_\kappa(u, v) \frac{\exp(-2hs)}{s^2} \quad (3.57a)$$

where $S_\kappa(u, v)$ is the spectrum of the susceptibility variation or the source spectrum and $\Gamma(u, v)$ is defined as

$$\Gamma(u, v) = (ju\alpha + jv\beta - s\gamma)(juI_x + jvI_y - sI_z) \quad (3.57b)$$

where $(\alpha, \beta$ and $\gamma)$ are direction cosines of the earth's field and I_x, I_y and I_z are the three components of the inducing magnetic field. For the sake of simplicity we assume that the random magnetization is uncorrelated, making its spectrum a constant and the direction of the inducing field is same as the current earth's magnetic field. Hence, $I_x = I_0\alpha$, $I_y = I_0\beta$, and $I_z = I_0\gamma$; Eq. (3.57b) reduces to

$$\begin{aligned} |\Gamma(u, v)|^2 &= I_0^2 [(s\gamma)^2 + (u\alpha + v\beta)^2]^2 \\ &= I_0^2 s^4 [\gamma^2 + (\alpha^2 + \beta^2)\cos^2(\theta - \theta_0)]^2 \end{aligned} \quad (3.58)$$

where θ_0 is the declination of the earth's field. Substituting Eq. (3.58) in Eq. (3.56), the spectrum of the total field is given by

$$S_{f_T}(u, v) = \exp(-2hs) I_0^2 s^4 [\gamma^2 + (\alpha^2 + \beta^2)\cos^2(\theta - \theta_0)]^2 \quad (3.59)$$

From Eq. (3.59) the angular spectrum may be expressed as

$$A_{\text{norm}}(\theta) = \Omega[\gamma^2 + (\alpha^2 + \beta^2)\cos^2(\theta - \theta_0)]^2 \quad (3.60)$$

where Ω is a constant. It may be noted that the angular spectrum is maximum in the direction of the polarization vector, as expected. This was actually verified by computing the angular spectrum of the total field observed on a plane two units above the horizontal layer (the total field is shown in Figure 3.25). The angles of declination and inclination of the polarizing vector are 37° east and 15° , respectively.

The computed angular spectrum and what is predicted in Ref. [6] are compared in Figure 3.26. Note that the theoretical results were derived under the assumption of white magnetization. Apart from the main peak in the computed angular spectrum corresponding to the direction of polarization, there are several sidelobes which are caused by square top prisms used in the modelling of the magnetic layer. The 2D source spectrum, $S_x(u,v)$ due to square top vertical prisms is like a star-shaped jelly fish which, when modulated with a $\Gamma(u,v)$ function defined in Ref. [6], gives rise to a complex structure of sidelobes including those at 0° and 90° shown in Figure 3.26. The sidelobes will disappear if we remove the geometrical pattern imposed by regular prisms and the angular spectrum will approach a smooth function predicted by theory.

3.6.2. Estimation of angular spectrum

The numerical computation of the radial and angular spectra requires averaging of the 2D spectrum over concentric rings and wedges as shown in Figure 3.2. Because of this averaging, the radial and angular spectra tend to be smooth functions. However, in the low frequency band the number of points in each angular wedge is highly variable causing increased variability in the estimated angular spectrum. This was overcome by converting the 2D spectrum from the rectangular grid to a polar raster using bilinear interpolation [21]. The resulting angular spectrum turns out to be smoother. An example of a smooth low frequency angular spectrum is shown in Figure 3.27.

The presence of a peak in the angular spectrum is an indication of the presence of a linear feature in the map but not always. Some peaks in the angular spectrum may be attributed to the source spectrum; for example, the peaks at 0° and 90° in Figure 3.26 are caused by the spectrum of square top prisms. From Eq. (2.84b) the source spectrum of a horizontal sheet of unit cubes with random susceptibility is obtained by combining all terms pertaining to the source shape and susceptibility,

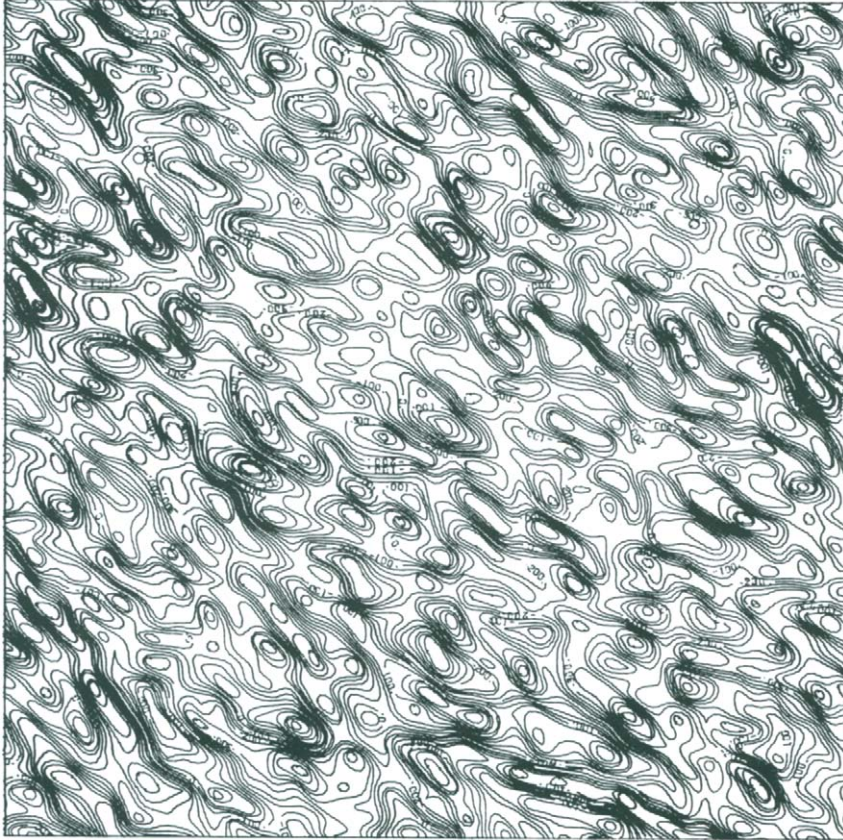


Figure 3.25. Total magnetic field due to a randomly magnetized horizontal layer.

$$S_{\kappa}(u, v) = \sigma_{\kappa}^2 \operatorname{sinc}^2(u) \operatorname{sinc}^2(v) (1 - \exp(-s))^2$$

A plot of above function is shown in Figure 3.28. The angular spectrum will show two small peaks along the u and v axes, that is, along 0° and 90° .

3.6.3. Orientation of a fault

We demonstrate the feasibility of estimating the direction of a fault from the angular spectrum. For this, consider the example of the faulted magnetized layer shown in Figure 3.29a. Only the deeper layer has a fault oriented at an angle of 45° (measured clockwise with respect to the North). The magnetic field due to this model is shown in Figure 3.29b. The magnetization is uniform, in the direc-

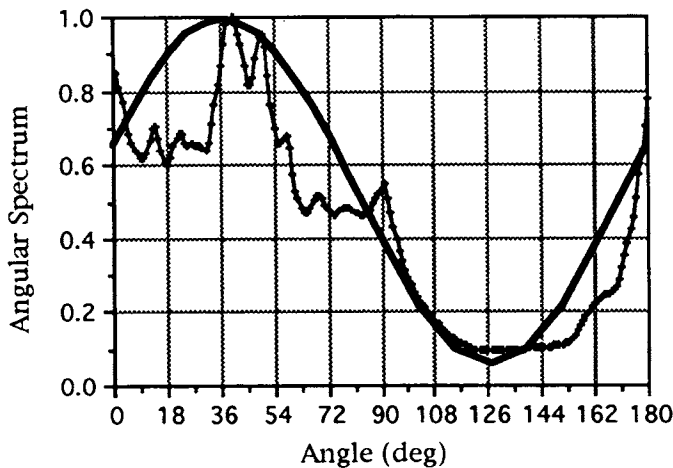


Figure 3.26. Angular spectrum of a magnetic field (total) due to a horizontal sheet made up of vertical prisms whose susceptibility is a uniformly distributed random variable in the range 0.0005–0.05, but the sheet is uniformly polarized (inclination 15° and declination 37° east). Theoretically the predicted angular spectrum is shown by a thick curve.

tion, declination = 5° and inclination = 15° throughout the model (this corresponds to the earth's magnetic field vector at Bangalore, India).

The presence of a fault in the lower layer is felt on the magnetic contours. Even an experienced interpreter would find it almost impossible to detect the fault from the magnetic map. In order to reveal the contribution of the faulted layer from below, we have plotted in Figure 3.30 the magnetic field due to the faulted layer alone. Notice the field contours running along the fault. This effect of the fault is responsible for the peak in the angular spectrum.

We have computed the radial and the angular spectra of the magnetic field matrix of size 128×128 . The spectrum, that is, magnitude square of the Fourier transform was computed first. Next, to compute the angular spectrum we averaged the two-dimensional spectrum over the angular sectors shown in Figure 3.2. The averaging was carried over two frequency bands, namely, the low frequency band (1–10 frequency numbers) and the high frequency band (11–35 frequency numbers). Note that the Nyquist frequency is at frequency number 64. The angular spectra is shown in Figure 3.31. It is clearly seen that the presence of a fault at the correct position is shown by a peak in the low frequency angular spectrum but the corresponding peak in the high frequency band is absent.

Other peaks in the angular spectrum, in particular the one at 90° , may be explained on the basis of direction of polarization, a tapered 2D window function used in the computation of the spectrum and the geometrical shape of the mag-

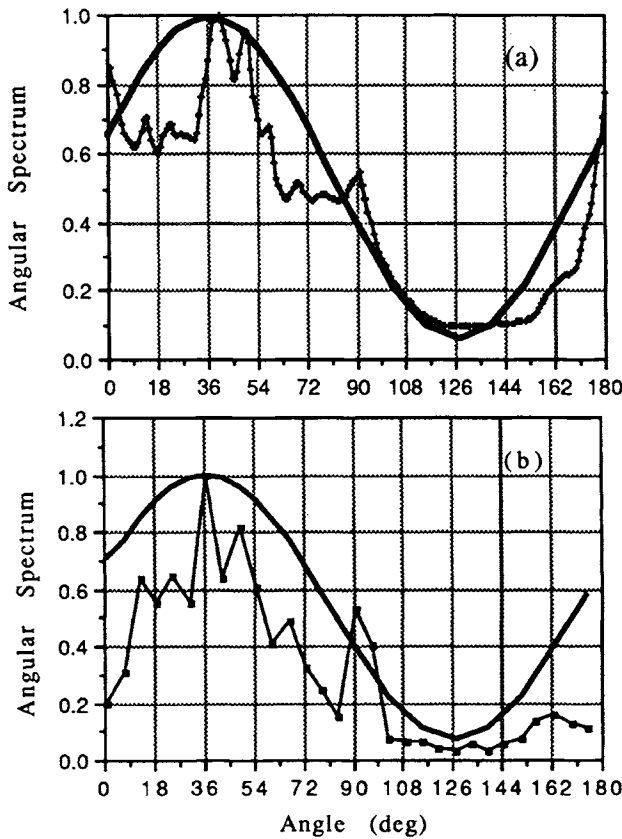


Figure 3.27. A comparison of angular spectra computed by averaging (a) over radial lines after conversion to a polar grid (Figure 3.26 is reproduced for convenience) and (b) over wedges as shown in Figure 3.2.

netized bodies. If the fault direction coincides with one of the horizontal edges of the rectangular prism, or the direction of polarization or is parallel to the edge of the data matrix, the angular spectra caused by the fault and the shape of the magnetized bodies will be similar. Then it is not possible to detect the fault. The effect of polarization may be removed by reducing the magnetic field to the pole and the effect of the tapered rectangular window may be isolated by rotating the map and repeating the processing.

3.6.4. Application to real data

The aeromagnetic map over the eastern part of the south Indian shield [22] was used for the present study. The map, shown in Figure 3.32, was digitized at 1 km interval. This resulted in a data matrix of 192×192 .

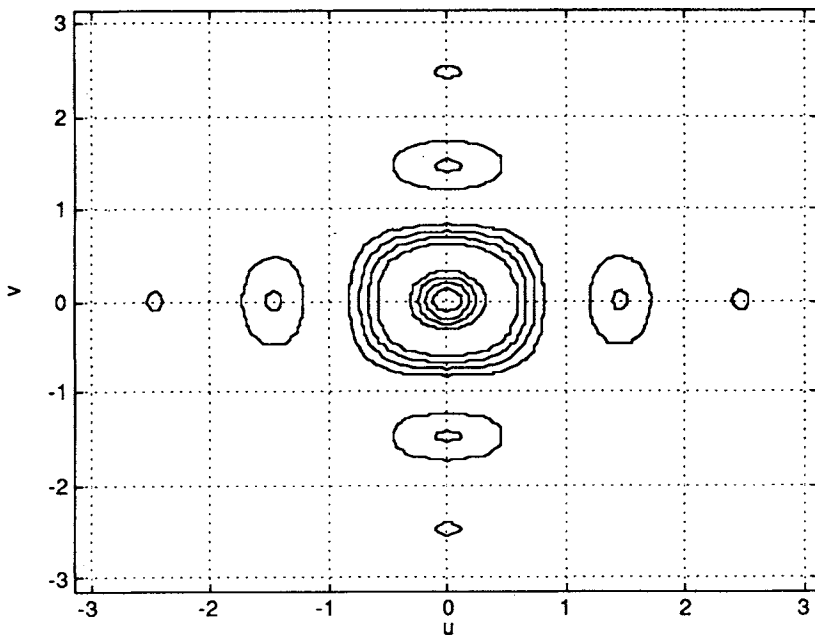


Figure 3.28. Averaged 2D spectrum of unit cubes with random susceptibility.

We computed both the radial and angular spectra. The results are shown in Figures 3.33 and 3.34. The radial spectrum seem to support the possibility of three linear segments as marked on the graph.

From the slopes of the segments at these points it may be inferred that the depths to the corresponding magnetic layers are 8.0, 3.0 and 1.1 km. The flight height in this survey was 1.5 km (above mean sea level). The depths to the magnetic layers with respect to the ground surface are 6.8 and 1.8 km and the third layer is probably due to surface rocks (surface is assumed to be 300 m above mean sea level). For the purpose of computing the angular spectrum the frequency band was divided into three sub-bands: a low frequency band 2–20 (frequency numbers); mid-frequency band 10–40; and a high frequency band 50–80. The angular spectra for all three sub-bands are shown in Figure 3.34.

The angular spectrum in the low frequency band has a prominent peak at 138° which corresponds to an east northeast west southwest fault suggested in Ref. [22; fault B4 in Figure 4]. The angular spectrum in the mid-frequency band also shows a peak corresponding to this fault but with considerably reduced magnitude. The high frequency angular spectrum, however, does not show these peaks. Instead there are other peaks which may be explained as follows. The peaks at 0° and 90° in all three bands are caused by the tapered rectangular window used in

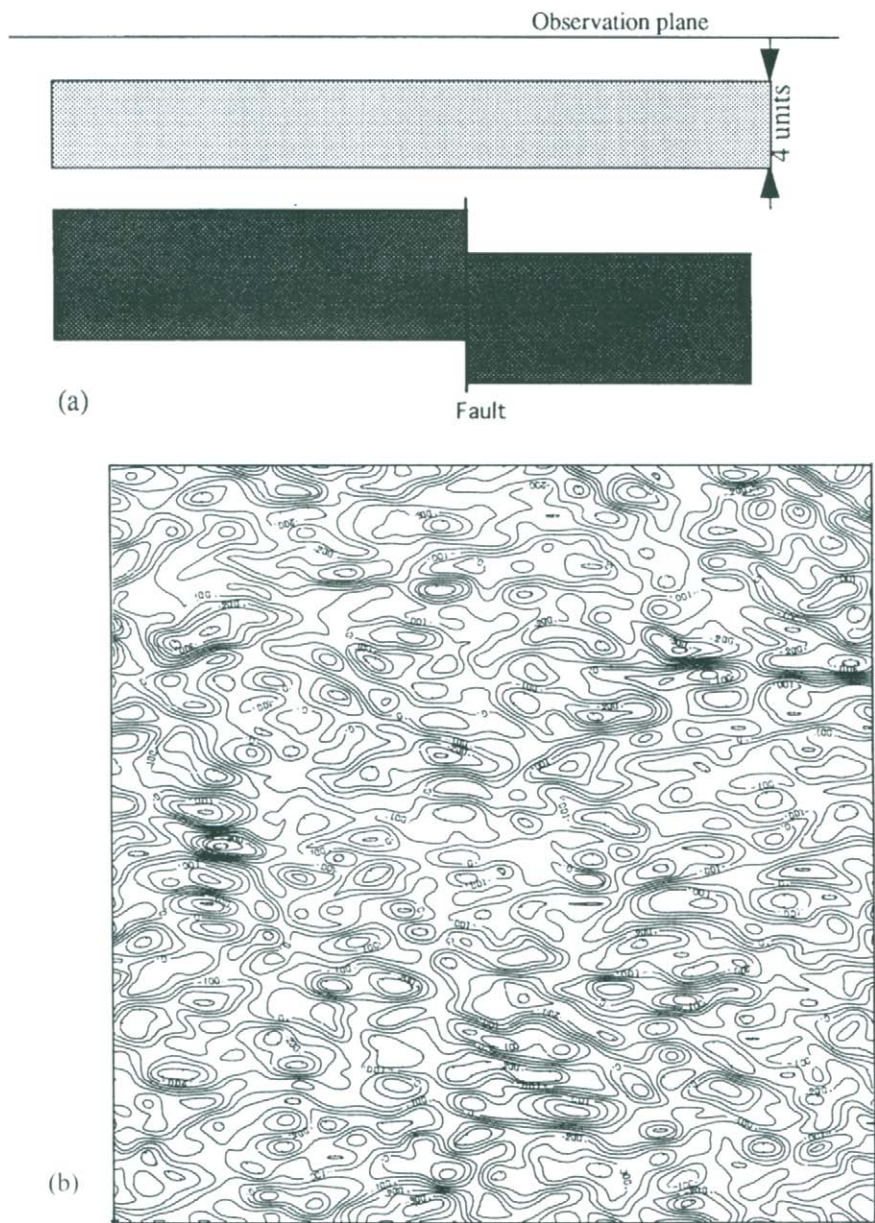
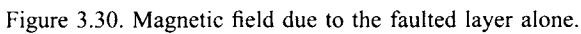


Figure 3.29. (a) A model of a faulted layer underlying a normal layer and (b) total magnetic field. spectrum estimation, the large peak at 175° in the low and mid-frequency bands corresponds to the direction of polarization, in the direction of the Earth's mag-



3.7. Coherence analysis

The gravity and magnetic fields due to rock formation are likely to be correlated particularly when the density and susceptibility variations are connected through a common influencing factor. Indeed we have shown in Chapter 2 (see Eq. (2.90)) how to map a gravity field into a magnetic field when the density and the susceptibility are constant within a body and zero outside. When the density and susceptibility are variable and the body is a thin sheet or a semi-infinite

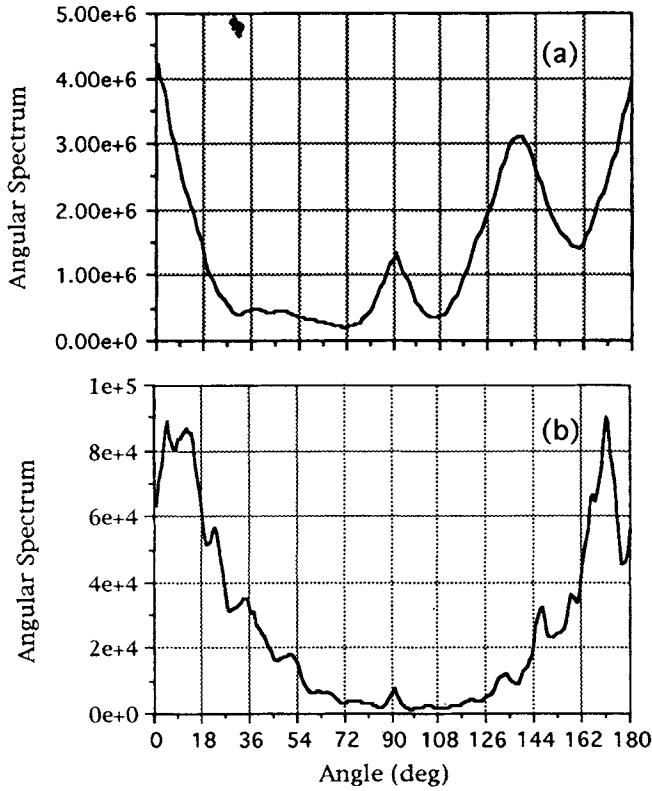


Figure 3.31. Angular spectrum showing the presence of a fault in the lower layer. (a) Angular spectrum in the low frequency band (1–10 frequency numbers); (b) angular spectrum in the high frequency band (11–35 frequency numbers).

medium the resulting gravity and magnetic field are related as in Eqs. (2.91) and (2.92), respectively.

3.7.1. Stochastic model for the density and susceptibility

Let us consider a stochastic model for the density and susceptibility variations, in particular, consider a thin sheet model and assume that

$$P(u, v, h) = H(u, v)K(u, v, h) + N(u, v) \quad (3.61)$$

where $H(u, v)$ is the transfer function and $N(u, v)$ is that part of the density varia-

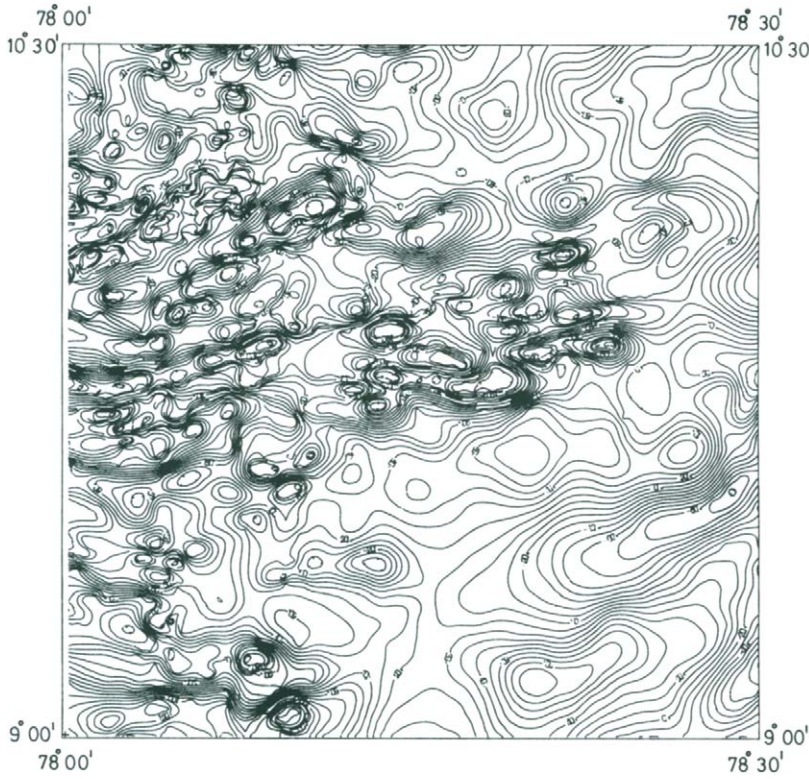


Figure 3.32. Aeromagnetic map over the eastern part of the south Indian Shield.

tions which are not related to the susceptibility variations. Using the above model in Eq. (2.91) we can compute the coherence between the resulting gravity field and the total magnetic field.

$$\begin{aligned}
 & E \left\{ \frac{1}{4\pi^2} dF_z(u, v, h) \frac{1}{4\pi^2} dF_T^*(u, v, h) \right\} \\
 &= \lambda^2 \frac{\Gamma^*(u, v)}{sG} E \{ [H(u, v) dK(u, v, h) + N(u, v)] dK^*(u, v, h) \} \\
 &= \lambda^2 \frac{\Gamma^*(u, v)}{sG} H(u, v) \frac{1}{4\pi^2} S_\kappa(u, v) du dv
 \end{aligned}$$

where we assumed that $N(u, v)$ is uncorrelated with $K(u, v, h)$. λ is an arbitrary

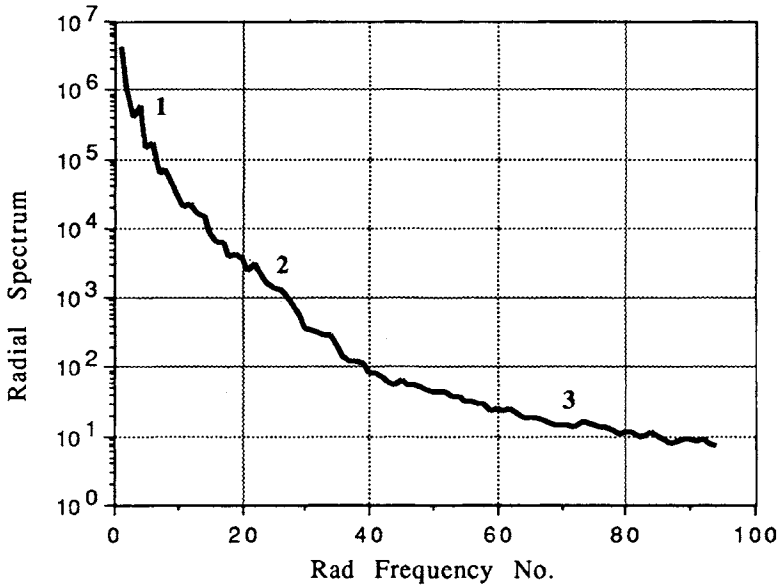


Figure 3.33. The radial spectrum of south Indian shield data. Three linear segments are marked. The depth estimated from the slopes are 8.0, 3.0 and 1.1 km, respectively. For the purpose of estimating the angular spectrum, the frequency band was divided into three subbands: low frequency, 2–20; mid-frequency, 10–40; and high frequency, 50–80 frequency numbers. The Nyquist frequency is at frequency number 96.

constant and $S_{\kappa}(u, v)$ is the spectrum of the susceptibility variations. Similarly we can obtain

$$\begin{aligned} & \mathbb{E} \left\{ \frac{1}{4\pi^2} dF_z(u, v, h) \frac{1}{4\pi^2} dF_z^*(u, v, h) \right\} \\ &= \lambda^2 |H(u, v)|^2 \frac{1}{4\pi^2} S_{\kappa}(u, v) du dv + \lambda^2 \frac{1}{4\pi^2} S_N(u, v) du dv \end{aligned}$$

and

$$\mathbb{E} \left\{ \frac{1}{4\pi^2} dF_T(u, v, h) \frac{1}{4\pi^2} dF_T^*(u, v, h) \right\}$$

$$= \lambda^2 \left| \frac{\Gamma(u, v)}{sG} \right|^2 \frac{1}{4\pi^2} S_{\kappa}(u, v) du dv$$

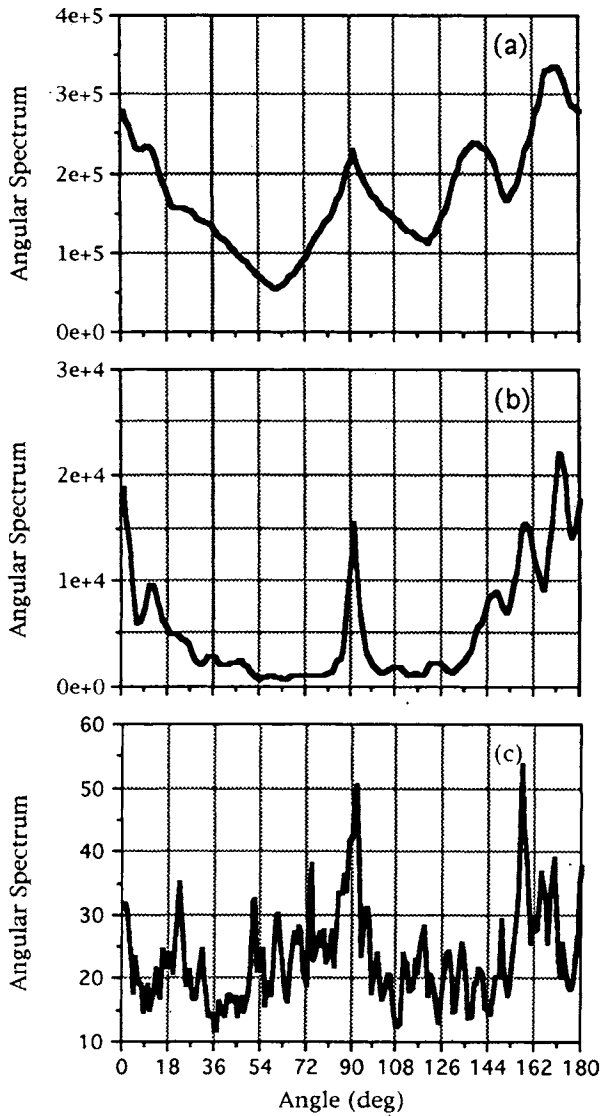


Figure 3.34. Angular spectrum over three different frequency bands. From the low frequency angular spectrum we infer that there is a major fault oriented at 48°. (a) Low frequency band; (b) mid-frequency band and (c) high frequency band.

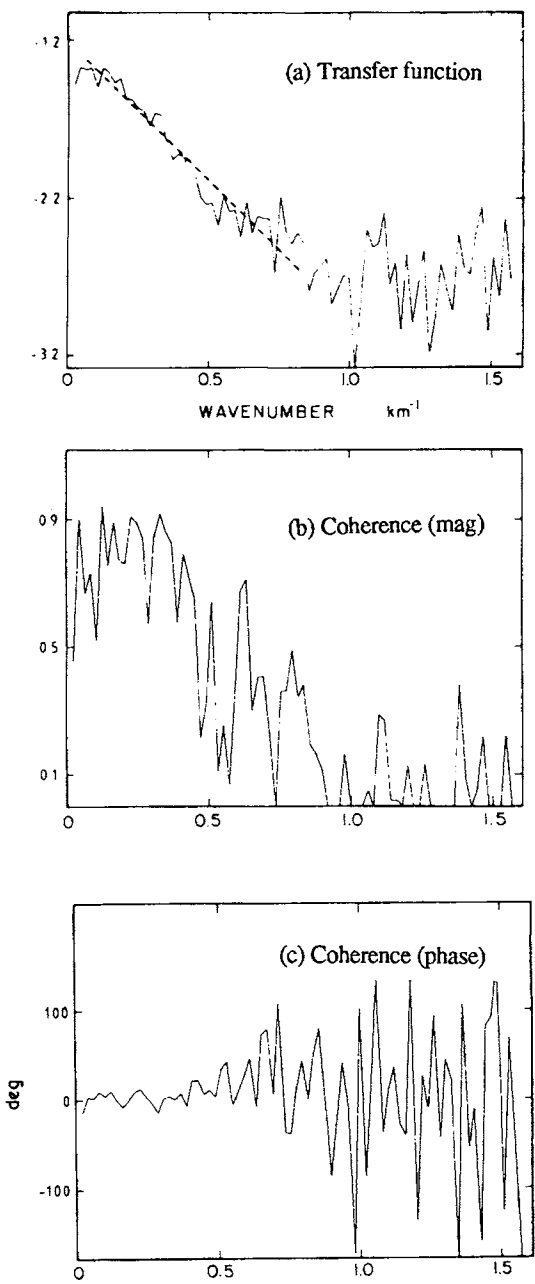


Figure 3.35. Coherence study of the gravity and topography across the Kane fracture zone [28]: (a) transfer function; (b) coherence magnitude; (c) coherence phase.

where $S_N(u, v)$ is spectrum of the residual component in the density variations. Following the definition of coherence (see Eq. (3.13)) we obtain

$$\begin{aligned} \text{coh}_{f_z f_T}(u, v) &= \frac{\mathbb{E} \left\{ \frac{1}{4\pi^2} dF_z(u, v, h) \frac{1}{4\pi^2} dF_T^*(u, v, h) \right\}}{\sqrt{\mathbb{E} \left\{ \frac{1}{4\pi^2} dF_z(u, v, h) \frac{1}{4\pi^2} dF_z^*(u, v, h) \right\} \mathbb{E} \left\{ \frac{1}{4\pi^2} dF_T(u, v, h) \frac{1}{4\pi^2} dF_T^*(u, v, h) \right\}}} \\ &= \frac{\frac{\Gamma^*(u, v)}{sG} H(u, v)}{\sqrt{(|H(u, v)|^2 + \frac{S_N(u, v)}{S_\kappa(u, v)}) \left| \frac{\Gamma(u, v)}{sG} \right|^2}} \end{aligned} \quad (3.62)$$

$|\text{coh}_{f_z f_T}(u, v)| = 1$ whenever $S_N(u, v)/S_\kappa(u, v) = 0$; that is, the magnetic and gravity field are completely correlated whenever the susceptibility variations are linearly related to the density variations. The model given in Eq. (3.61) was first proposed in Ref. [25] but its demonstration on real data is not very convincing. Significant correlation between the Earth's gravitational field and the non-dipole part of the geomagnetic field was reported in Ref. [26].

3.7.2. Isostatic compensation

A topographic surface not only produces its own gravity and magnetic fields, which are naturally correlated, but also influences the density variations deep inside the crust, a phenomenon known as isostatic compensation [27,28]. The gravity and topography are modelled as in Eq. (3.61). An example of coherence between the gravity and bathymetry profiles perpendicular to the Kane fracture zone of the mid-Atlantic ridge is shown in Figure 3.35, taken from [28].

References

- [1] C. W. Horton, W. B. Hemphkin and A. A. J. Hoffman, A statistical analysis of some aeromagnetic maps for northwestern Canadian shield, *Geophysics*, 29, 582–601, 1964.
- [2] Von Wolfgang Mundt, Anwendung statischer verfahren in der magnetik und gravimetrie zur Tiefenerkunden, *Pure Appl. Geophys. (Pageoph.)*, 69, 143–157, 1968.
- [3] A. M. Yaglom, *An Introduction to Theory of Stationary Random Functions*, Prentice Hall, Englewood Cliffs, NJ, 1962.
- [4] P. S. Naidu, *Modern Spectrum Analysis of Time Series*, CRC Press, Boca Raton, FL, 1996.
- [5] S. M. Kay, *Modern Spectrum Analysis*, Prentice Hall, Englewood Cliffs, NJ, 1989.

- [6] R. E. Sheriff, *Geophysical Methods*, Prentice Hall, Englewood Cliffs, NJ, 1989.
- [7] F. J. Harris, On the use of windows for harmonic analysis with discrete Fourier transform, *Proc. IEEE*, 66 (1), 51–83, 1978.
- [8] D. J. Thompson, Spectrum estimation and harmonic analysis, *Proc. IEEE*, 70 (9), 1055–1096, 1982.
- [9] C. Runge and H. König, *Die Grundlehren der mathematischen Wissenschaften, Vorlesungen über Numerisches Rechnen*, Vol. 11, Springer-Verlag, Berlin, 1924.
- [10] W. Tukey and J. W. Cooley, An algorithm for machine calculation of complex Fourier series, *Math. Comput.*, 19, 297–301, 1965.
- [11] P. S. Naidu, FFT of externally stored data, *IEEE Trans., ASSP-26*, 473, 1970.
- [12] G. Rivard, Direct fast Fourier transform of bivariate functions, *IEEE Trans., ASSP-25*, 250–252, 1977.
- [13] H. J. Nussbaumer, *Fast Fourier Transform and Convolution Algorithm*, Springer-Verlag, Berlin, 1981.
- [14] P. S. Naidu, Estimation of spectrum and cross-spectrum of aeromagnetic field using fast digital Fourier transform (FDFT) techniques, *Geophys. Prosp.*, 17, 344–361, 1969.
- [15] M. J. Hinich and C. S. Clay, The application of the discrete Fourier transform in the estimation of power spectra, coherence, bispectra of geophysical data, *Rev. Geophys.*, 6, 347–363, 1968.
- [16] P. S. Naidu, Spectrum of potential fields due to randomly distributed sources, *Geophysics*, 33, 337–345, 1968.
- [17] P. S. Naidu, Stochastic modelling in gravity and magnetic interpretation, *J. Assoc. Exploration Geophys.*, 4, 1–11, 1983.
- [18] M. Pilkington and J. P. Todoeschuck, Fractal magnetization of continental crust, *Geophys. Res. Lett.*, 20, 627–630, 1993.
- [19] S. Maus and V. P. Dimri, Potential field power spectrum inversion for scaling geology, *J. Geophys. Res.*, 100, B7, 12605–12616, 1995.
- [20] I. G. Klushin, Investigation of the depth distribution of sources of gravitational and magnetic anomalies, *Bull. (Izv.) Acad. Sci. USSR Geophys. Ser.*, 9, 18–23, 1959.
- [21] A. C. Kak, Tomographic Imaging with diffracting and nondiffracting sources, in: S. Haykin (Ed.), *Array Signal Processing*, Prentice Hall, Englewood Cliffs, NJ, pp. 351–428, 1985.
- [22] A. G. B. Reddy, M. P. Mathew, B. Singh and P. S. Naidu, Aeromagnetic evidence of crustal structure in the granitic terrain of Tamilnadu-Kerala, *J. Geol. Soc. India*, 32, 368–381, 1988.
- [23] P. S. Naidu and M. P. Mathew, Angular spectrum for detection of a fault, *J. Geophys.*, 18, 189–194, 1997.
- [24] B. H. Jacobsen, A case for upward continuation as a standard separation filter for potential field maps, *Geophysics*, 52, 1138–1148, 1987.
- [25] M. Muniruzzaman and R. J. Banks, Basement magnetization estimates by wavenumber domain analysis of magnetic and gravity maps, *Geophys. J.*, 97, 103–117, 1989.
- [26] R. Hide and S. R. C. Malin, Novel correlation between global features of the earth's gravitational and magnetic fields, *Nature*, 225 (5233), 605–609, 1970.
- [27] L. M. Dorman and B. T. R. Lewis, Experimental isostasy, 1. Theory of the determination of the earth's isostatic response to a concentrated load, *J. Geophys. Res.*, 75, 3357–3365, 1970.
- [28] K. E. Loudon and D. W. Forsyth, Crustal structure and isostatic compensation near the Kane fracture zone from topography and gravity measurements – I Spectral analysis approach, *Geophys. J. R. Astr. Soc.*, 68, 725–750, 1982.
- [29] A. Papoulis, *Signal Analysis*, McGraw-Hill, New York, 1977.